ICARUS **123,** 503–523 (1996)
ARTICLE NO. 0175

Circumplanetary Dust Dynamics: Effects of Solar Gravity, Radiation Pressure, Planetary Oblateness, and Electromagnetism

DOUGLAS P. HAMILTON

University of Maryland, College Park, Maryland 20742-2421
E-mail: hamilton@astro.umd.edu

AND

ALEXANDER V. KRIVOV

Astronomical Institute, St. Petersburg University, St. Petersburg, Russia

Received December 18, 1995; revised March 25, 1996

We consider the motions of circumplanetary objects perturbed simultaneously by solar gravity, radiation pressure, planetary oblateness, and electromagnetic forces. Confining ourselves to the planar case, but retaining all nonlinear terms in the eccentricity, we rewrite the orbit-averaged equations for the sum of the four perturbations as a semicanonical system. We derive a conserved integral of the motion which is valid for initially elliptic orbits of arbitrary size and shape. This integral is used to investigate the phase space qualitatively and to show how the eccentricity and apses line evolve for various strengths of the perturbation forces. We find several different classes of motion and show that near certain critical initial conditions, small variations in parameters such as particle size or initial semimajor axis can cause dramatic changes in a particle's orbit. This effect is important in Saturn's E ring and for Phobos dust. We apply our model to dusty ejecta launched from several moons—Phobos, Deimos, Elara, and Enceladus—and to the motions of Elara itself. In each case, we compare our analytic results to numerical integrations of the full Newtonian equations of motion.

1. STATEMENT OF THE PROBLEM

Circumplanetary dust grains are affected by a large array of perturbation forces whose relative strengths vary significantly from one situation to another. In many applications, a single perturbation dominates over all others, and the resulting orbital dynamics are well approximated by neglecting the weaker forces. In such situations, analytic solutions are often possible, as exemplified by those for the orbital precessions induced by planetary oblateness (Danby 1988) and for the effects of radiation pressure (Mignard and Hénon 1984, Richter and Keller 1995). In other applications, however, several orbital perturbations are similar in strength, which greatly complicates the resulting orbital dynamics. Analytic approaches to these problems have been limited to cases where orbital eccentricities remain small. The interplay between like-sized perturbations, however, is particularly rich when orbital eccentricities are large, and large eccentricities are expected in many applications, including micrometer grains in Saturn's E ring (Horányi *et al.* 1992, Hamilton 1993), larger dust particles around Mars (Hamilton 1996, Ishimoto 1996, Juhász and Horányi 1995, Krivov *et al.* 1996a,b), and objects at extreme distances from all central bodies (Hamilton and Burns 1991,1992). In this paper, we analytically and numerically address the complicated motions of these highly eccentric orbits under the influence of multiple perturbation forces.

After planetary gravity, the strongest forces acting on circumplanetary dust grains are: (i) solar tides (ST), (ii) solar radiation pressure (RP), (iii) planetary oblateness (J2), and (iv) electromagnetism (EM). In almost all applications, one or more of these four forces dominates the perturbations to Keplerian motion about a planet. The first force is important for the orbits of grains far from planets, while the latter two dominate in the near zone. All four forces may be simultaneously important at intermediate distances. We now introduce some simplifications and then briefly discuss each of these forces in turn.

In order to make the problem more tractable, we limit ourselves to the planar problem; i.e., we assume that orbital motion is confined to two spatial dimensions. This simplification allows us to retain all terms in the orbital eccentricity unlike most other analytic studies. Two-dimensional motion holds rigorously only when the dust particle's orbital plane, the planet's orbital plane, and the planet's equatorial plane all coincide. Since most sources of circumplanetary

0019-1035/96 $18.00

dust have fairly low inclinations relative to the Laplace plane—the dynamical compromise between a planet's equatorial and its orbital planes—this 2D model is likely to be a good approximation of reality for planets with reasonably low obliquities. We also assume that the planets follow circular orbits around the Sun and average the perturbations to a dust grain's orbit over a single circuit about the central planet.

Solar gravity influences the motion of planetary grains by imparting unequal accelerations to the central planet and a nearby particle. We consider only the largest effects which are due to the so-called tidal term (Hamilton and Burns 1991). Higher-order solar terms are at least 10–100 times weaker, and perturbations from distant planets are ~1000 times smaller so both can be safely neglected.

For radiation pressure, we assume a spherical dust grain with uniform density and scattering properties (see Burns *et al.* 1979) and make the parallel-ray approximation (the strength and direction of radiation pressure are assumed not to vary over the dust grain's orbit). We neglect reflection from the central planet and the effects of the planetary shadow, both of which produce changes at least an order of magnitude weaker than those produced by direct solar illumination.

The dominant perturbation in the multipole expansion of a planet's nonspherical mass distribution is the axisymmetric quadrupole term parameterized by J_2 (Danby 1988). This J_2 component is 10–100 times larger than all other terms in the multipole expansion for all planets except slowly rotating Mercury and Venus. We neglect all other terms in the multipole expansion as well as gravity from planetary satellites. Although secular perturbations from satellites can be crudely approximated by an effective J_2, these should really be treated more carefully (see, e.g., Borderies *et al.* (1983), who derive secular equations valid for small eccentricities). Resonant perturbations cannot be treated with our method.

Electromagnetic forces on circumplanetary particles arise from the relative velocity between a charged dust grain and a spinning planetary magnetic field. We assume that the dust grain carries a constant charge and that the magnetic field is dipolar, corotating with the planet, and aligned with the planetary spin axis. This is an excellent approximation for Saturn and is a reasonable one away from the locations of Lorentz resonances for the Earth and Jupiter (Hamilton 1994). The magnetic fields of Uranus and Neptune are highly irregular within a few radii of these planets, which limits our approach to more distant orbits.

Finally, we ignore all slowly acting forces such as Poynting–Robertson drag and plasma drag. This limits our approach to short-term investigations of ~1000 years, which is not a serious handicap since typical grain lifetimes are often of this order.

In the next section, we derive an integral of the motion valid for 2D orbital evolution forced by solar gravity, radiation pressure, planetary oblateness, and electromagnetism. We then apply the integral to dust on distant orbits in Section 3, to dust near planets in Section 4, and to the most general case of dust at intermediate distances in Section 5. Section 6 provides a short summary of our results.

2. DERIVATION OF THE INTEGRAL OF THE MOTION

2.1. Variables and Force Parameters

There are four orbital elements that define a planar Keplerian orbit: the semimajor axis a, the eccentricity e, the longitude of pericenter $\tilde{\omega}$ (which is measured from an inertial reference point), and the mean anomaly M. With our neglect of drag forces and shadowing by the planet, the semimajor axis does not change in the orbit-averaged approximation. In addition, the perturbations to the mean anomaly describe only how fast a particle completes an orbit about the planet and are not of interest in our current effort.

Thus only the eccentricity and longitude of pericenter remain to be considered. Since the only "special" longitude in our two-dimensional problem is the solar longitude $\lambda_\odot$, we choose to measure the location of the pericenter from this reference. Hence we define the solar angle $\phi_\odot \equiv \tilde{\omega} - \lambda_\odot$ and use this angle instead of $\tilde{\omega}$. We also take $\lambda_\odot$ as the independent variable to make our differential equations dimensionless. Since the planetary orbit is assumed to be circular, $\lambda_\odot = n_\odot t$ is a linear function of time t, where $n_\odot$ is the planet's mean motion about the Sun.

For each of the four disturbing forces, we introduce a dimensionless parameter describing the perturbation strength. These four parameters depend on physical properties of the planets and of the dust, and also on the particle's semimajor axis.

For the solar tidal force, we define the *tidal parameter* A by

$$A \equiv \frac{3}{4}\frac{n_\odot}{n}, \tag{1}$$

where $n = (\mathrm{GM}/a^3)^{1/2}$ is the mean motion of the particle, and GM is the planet's gravitational constant. The constant A is positive and, for bound orbits, ranges between zero and roughly unity.

We define the *radiative parameter* C by

$$C \equiv \frac{3}{2}\frac{n}{n_\odot}\sigma, \tag{2}$$

which is equivalent to $\alpha/n_\odot$ in the notation used by other authors, e.g., Hamilton (1993). Here, σ is the ratio of the

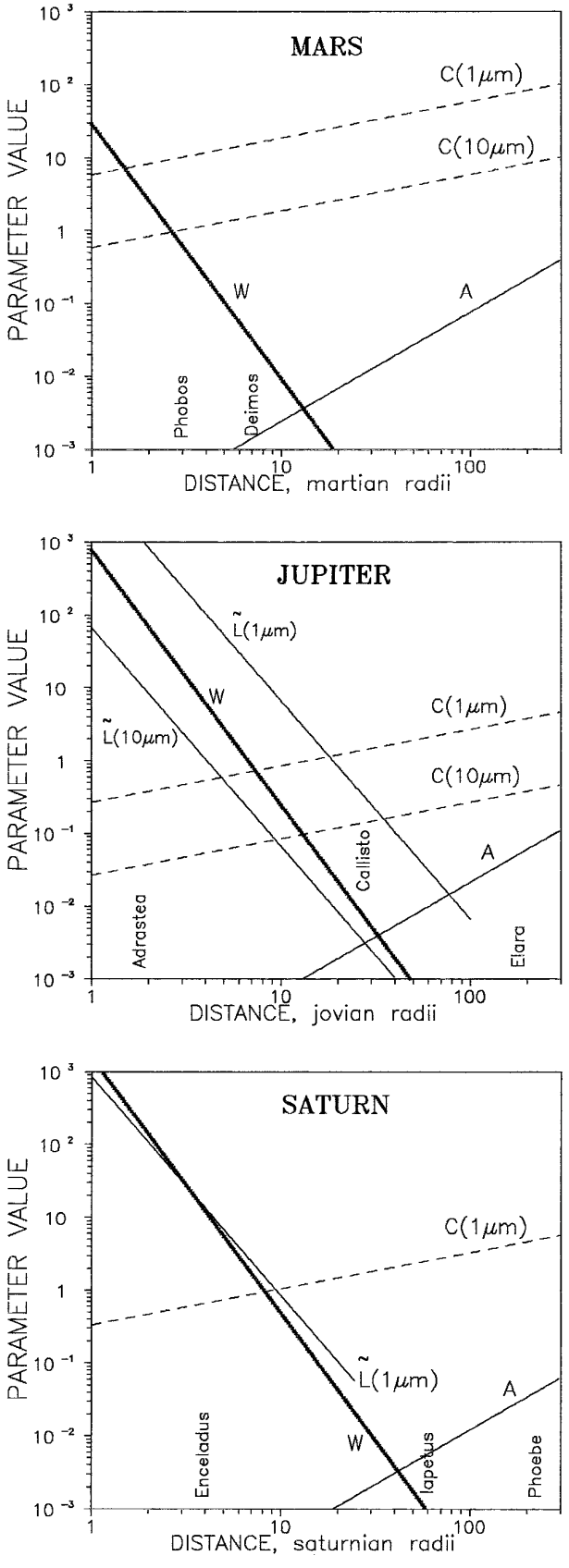

radiative force to the planet's gravity for a circular orbit at distance a:

$$\sigma = \frac{F_{\rm rp}}{F_{\rm gr}} = \frac{3}{4} Q_{\rm pr} \frac{F_\odot a^2}{{\rm GM}c\rho_{\rm g} r_{\rm g}}. \tag{3}$$

In Eq. (3), $Q_{\rm pr}$ is the radiation pressure efficiency factor, $F_\odot$ is the solar flux at the heliocentric distance of planet, c is the speed of light, and $r_{\rm g}$ and $\rho_{\rm g}$ are the radius and material density of the particle. Like A, C is positive and ranges between zero and about one.

The *oblateness parameter* W is introduced as

$$W \equiv \frac{3}{2} J_2 \left(\frac{R}{a}\right)^2 \frac{n}{n_\odot}, \tag{4}$$

where J_2 and R denote the second zonal harmonic coefficient and the equatorial radius of the planet, respectively. The oblateness parameter is always positive.

Finally, the *Lorentz parameter* $\tilde{L}$ is defined by

$$\tilde{L} \equiv 2 \frac{n}{n_\odot} \frac{n}{\Omega_{\rm p}} L, \tag{5}$$

where $\Omega_{\rm p}$ is angular velocity of planet's rotation (and that of magnetic field rotation), and L is Hamilton's (1993) parameter,

$$L \equiv \frac{Q_{\rm g} B_0 R^3 \Omega_{\rm p}}{{\rm GM}c m_{\rm g}}. \tag{6}$$

Here $m_{\rm g}$ and $Q_{\rm g}$ are the grain's mass and charge, and B_0 is the magnetic strength at the planetary equator. Note that the sign of L (and $\tilde{L}$) may be either positive or negative, depending on the sign of the grain's charge. Physically, $|L|$ is the ratio of the Lorentz force $F_{\rm em}$ to the planet's gravitational force (evaluated for a particle placed in the equatorial plane and motionless with respect to an inertial frame); L is independent of distance from the primary.

Figure 1 shows the variation of these parameters as a function of distance from Mars, Jupiter, and Saturn. The relative sizes of these parameters, and hence the strengths of the perturbation forces, vary strongly with grain size

FIG. 1. Plots of the dimensionless force parameters for Mars, Jupiter, and Saturn. Each plot presents, as a function of distance, numerical values of the four perturbation parameters: A (solar tides, ST), C (radiation pressure, RP), W (planetary oblateness, J2), and $\tilde{L}$ (Lorentz Force, EM). For Mars, Jupiter, and Saturn we assume densities $\rho_{\rm g}$ of 2.0, 1.0, and 1.0 g cm^{-3}, and voltages $\Phi_{\rm g}$ of 0, 5, and -5 V, respectively. We truncate the curve for $\tilde{L}$ at the edge of the respective planetary magnetospheres, which we take to be 1, 100, and 20 planetary radii for Mars, Jupiter, and Saturn.

and distance from the primary. For all planets, both electromagnetism and the oblateness force drop off rapidly with increasing distance. In contrast, radiation pressure and the solar tidal force are stronger perturbations farther from the planet. This behavior allows us to identify three dynamical zones: the ''far'' zone where oblateness and electromagnetism can be neglected, the ''near'' zone where the solar tidal force is negligible, and an ''intermediate'' zone where all forces may need to be considered.

2.2. Equations of Motion

As discussed in the previous section, we confine ourselves in this paper to a two-dimensional problem in which the equations of motion have been averaged over one particle orbit about the primary. Despite this restriction, 2D orbits still display non-trivial behavior, periodically shifting between circles and ellipses which spin in space. In Fig. 2, we show numerically determined maximum eccentricities attained by dust grains of various sizes launched with low initial velocities from Deimos, Phobos, and Enceladus. There are strong differences in these curves, which indicates the influence of interesting dynamical processes. An understanding of these curves, and especially of the sharp drops in eccentricity for Phobos and Enceladus particles, is one of our motivations for undertaking this study.

We begin analytically by obtaining the orbit-averaged equations for e and $\phi_\odot$ valid for prograde $i = 0$ particles:

$$\frac{d\phi_\odot}{d\lambda_\odot} = A\sqrt{1-e^2}\,[1 + 5\cos(2\phi_\odot)] + C\frac{\sqrt{1-e^2}}{e}\cos\phi_\odot + \frac{W}{(1-e^2)^2} + \frac{\tilde{L}}{(1-e^2)^{3/2}} - 1 \tag{7}$$

$$\frac{de}{d\lambda_\odot} = 5Ae\sqrt{1-e^2}\sin(2\phi_\odot) + C\sqrt{1-e^2}\sin\phi_\odot.$$

These equations come from those of Hamilton (1993), to which the additional solar tidal terms have been added (e.g., Duboshin 1976, Eq. (6.4.35)). The equations of motion are relative to a coordinate frame centered on the planet and rotating with the planet's mean motion about the Sun. In this frame, the Sun is motionless. Equations relative to a nonrotating frame are obtained by adding one to the first of Eqs. (7).

Ideally, we would like to solve system (7) analytically. This has been accomplished for several special cases, most notably oblateness alone (see Danby 1988) and radiation pressure alone (see Mignard and Hénon 1984, Hamilton and Burns 1992, Juhász and Horányi 1995, Richter and Keller 1995). Adding electromagnetism to the oblateness problem does not change the character of the solution, and, for small eccentricities, there is even an approximate solution valid when radiation pressure, oblateness, and electromagnetism are simultaneously important (Horányi *et al.* 1992). Here, however, we study the most general 2D

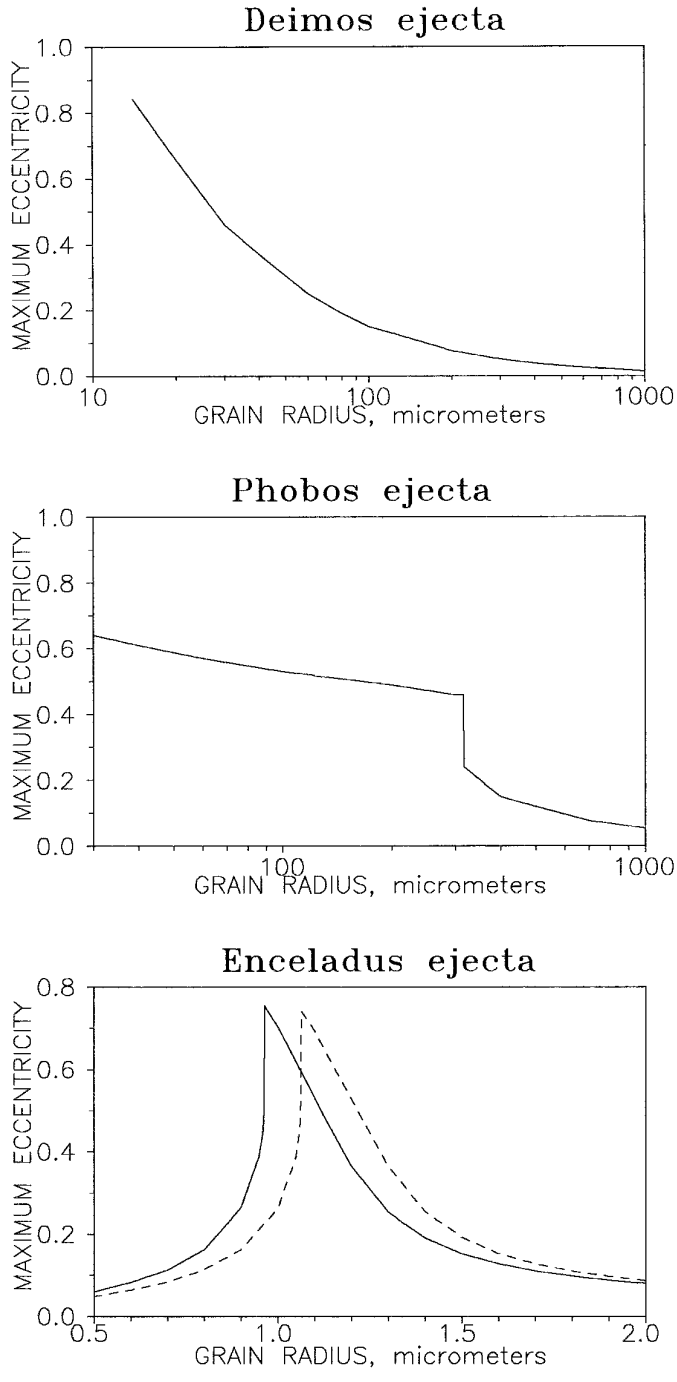

FIG. 2. Maximum eccentricity attained by initially circular orbits as a function of dust grain radius for Deimos ejecta, Phobos ejecta, and Enceladus ejecta (saturnian E ring particles). These curves come from integration of the 2D equations (7). Note the differences in the three graphs, especially the sharp drops in the last two. The solid and dashed lines in the final graph are for electromagnetic potentials of $\Phi_g = -5$ V and $\Phi_g = -6$ V, respectively.

problem in which all four forces are present and, moreover, eccentricities may take on all values $0 \le e \le 1$.

Although a full solution to Eqs. (7) in terms of elementary functions probably does not exist, we can find an exact integral of the motion. The trick is to write system (7) in the semicanonical form

$$\frac{de}{d\lambda_\odot} = -\frac{\sqrt{1-e^2}}{e}\frac{\partial \mathscr{K}}{\partial \phi_\odot}, \quad \frac{d\phi_\odot}{d\lambda_\odot} = \frac{\sqrt{1-e^2}}{e}\frac{\partial \mathscr{K}}{\partial e}, \tag{8}$$

with the "Hamiltonian"

$$\mathscr{K} = \sqrt{1-e^2} + \frac{1}{2}Ae^2[1 + 5\cos(2\phi_\odot)] + Ce\cos\phi_\odot + \frac{W}{3(1-e^2)^{3/2}} + \frac{\tilde{L}}{2(1-e^2)}. \tag{9}$$

The integral of the motion is then given by

$$\mathscr{K}(e, \phi_\odot) = \text{Const}, \tag{10}$$

and all valid particle trajectories are confined to move along lines of constant $\mathscr{K}(e, \phi_\odot)$. Note that the Hamiltonian has reflection symmetry $\mathscr{K}(e, \phi_\odot) = \mathscr{K}(e, -\phi_\odot)$.

The advantageous idea to rewrite the equations in the form of Eq. (8) was first proposed by K. V. Kholshevnikov (private communication) for studying the forces of radiation pressure and oblateness (see also Krivov *et al.* (1996b), who applied this technique to martian dust). The generalization of the idea to include solar tidal and electromagnetic perturbations is straightforward. We note also that the equations may be put into fully canonical form with the transformation $\Psi = (1 - e^2)^{1/2}$.

The existence of an integral of the motion is perhaps not so surprising considering the fact that the forces due to solar tides, radiation pressure, and oblateness may all be derived from potentials. In fact, if we omit electromagnetism, Eq. (9) is a modified version of Tisserand's criterion which includes the effects of oblateness and radiation pressure, and constrains the particle to remain near the planet. What is surprising is that electromagnetic forces can be included too, and that Eq. (9) takes on such a simple form after averaging over an orbit. The integral's existence has a number of important consequences. First, it reduces a system with two unknown variables—$e(t)$ and $\phi_\odot(t)$—to one with a single unknown $\phi_\odot(t)$. Knowledge of $\phi_\odot(t)$ and Eqs. (9) and (10) determine $e(t)$. In addition, curves of constant $\mathscr{K}(e, \phi_\odot)$ plotted in the $(e, \phi_\odot)$ plane must be closed, and hence all orbits are periodic. Although a small number of orbits have infinite period, most orbits must return to their exact starting conditions after a finite amount of time. The integral given by Eqs. (9) and (10) determines, for given initial conditions, a closed level curve consisting of all possible states in $(e, \phi_\odot)$ space where the orbit will be found at future times. The unknown variable, for which we have no analytic integral, tells exactly when these states occur and gives the period required to move around the level curve. This information is usually less interesting for practical applications, especially for rings composed of large ensembles of particles.

Writing Eqs. (7) in semicanonical form greatly simplifies the qualitative study of their solutions. The properties of these solutions are essentially determined by stationary points of the Hamiltonian $\mathscr{K}$ defined as

$$\frac{\partial \mathscr{K}}{\partial e} = \frac{\partial \mathscr{K}}{\partial \phi_\odot} = 0. \tag{11}$$

The stationary points of $\mathscr{K}$ are identical to those of Eqs. (7) except when $e = 0$ and $e = 1$ (see Eq. (8)). These special cases will need to be considered separately. For the general case when $0 < e < 1$, however, we use the Hamiltonian formalism to investigate the existence and stability of fixed points.

We collect terms independent of $\phi_\odot$ from the first of Eqs. (7) in the function $\mathscr{K}_0(e)$, defined as

$$\mathscr{K}_0(e) \equiv \frac{e}{\sqrt{1-e^2}}\left[\frac{W}{(1-e^2)^2} + \frac{\tilde{L}}{(1-e^2)^{3/2}} - 1\right], \tag{12}$$

so that the derivatives of the Hamiltonian may be written

$$\frac{\partial \mathscr{K}}{\partial e} = \mathscr{K}_0(e) + Ae[1 + 5\cos(2\phi_\odot)] + C\cos\phi_\odot,$$
$$\frac{\partial \mathscr{K}}{\partial \phi_\odot} = -5Ae^2\sin(2\phi_\odot) - Ce\sin\phi_\odot. \tag{13}$$

Since $\mathscr{K}_0(0) = 0$, two stationary points of $\mathscr{K}$ always exist:

$$P_1 = \left(0, \frac{\pi}{2}\right), \quad P_2 = \left(0, \frac{3\pi}{2}\right). \tag{14}$$

In the Hamiltonian problem, the presence of radiation pressure ensures that P_1 and P_2 are always saddle points since

$$\frac{\partial^2 \mathscr{K}}{\partial e^2}\frac{\partial^2 \mathscr{K}}{\partial \phi_\odot^2} - \left(\frac{\partial^2 \mathscr{K}}{\partial e \partial \phi_\odot}\right)^2 = -C^2 \le 0. \tag{15}$$

Because these stationary points have $e = 0$, however, they need not be fixed points of the original problem, and indeed they are not as can be easily checked in Eqs. (7). Nevertheless, the points are physically meaningful: radiation pres-

sure causes orbits with very tiny eccentricities to precess or regress rapidly away from P_2 toward P_1.

The other special case, $e = 1$, corresponds to an unphysical orbit that passes through the center of the planet. It is easy to see that there are no fixed points with $e = 1$ in either the original or the Hamiltonian problem.

The number, locations, and stability of additional fixed points depend in a complicated way on the values of the parameters A, C, W, and $\tilde{L}$. Rather than attacking the full problem directly, we separate the space surrounding a planet into three distinct regimes—the far zone, the near zone, and the intermediate zone—and discuss each of these separately. The advantage of this approach is that in certain applications we may neglect some of the perturbing forces, thereby simplifying the analysis. Figure 1 shows that oblateness and electromagnetism are negligibly small for distant orbits while the solar tidal force can be ignored closer to the planet. In each of the next three sections, we first treat a simplified problem analytically, and then give numerical examples in the Solar System where the analysis applies. In this manner, we progress from straightforward problems to more complicated ones, eventually returning to discuss the full Hamiltonian.

3. THE FAR ZONE

For orbits far from the central planet, both oblateness and electromagnetism are unimportant (see Fig. 1) so we can set $W = \tilde{L} = 0$. We focus first on small particles micrometers to tens of micrometers in size which are dominated by radiation pressure.

3.1. Radiation Pressure Only (RP)

With $W = \tilde{L} = A = 0$, Eqs. (11)–(13) admit one stationary point with $e \neq 0$. The point is given by $P_{\rm RP} = (e_{\rm RP}, 0)$, where $e_{\rm RP}$ is obtained from $\mathscr{K}_0(e) = -C$:

$$e_{\rm RP} = \frac{C}{\sqrt{1 + C^2}}. \tag{16}$$

The point $P_{\rm RP}$ corresponds to an orbit with a constant eccentricity that always keeps its pericenter oriented toward the Sun. The value of $e_{\rm RP}$ is bounded between zero and one, which indicates that this orbital solution exists for arbitrarily strong radiation pressure (as long as the approximation for orbit-averaging is satisfied). Examining the second derivatives of $\mathscr{K}$ shows that $P_{\rm RP}$ is always a local maximum.

As an example, we consider Deimos ejecta. The bombardment of martian satellites by interplanetary micrometeoroids is believed to cause continuous ejection of regolith material into nearly circular orbits about Mars. This ejecta should form dust tori along the orbits of the martian moons (Soter 1971). The detailed dynamics of such ejecta have been considered by many authors, including Hamilton (1996), Ishimoto (1996), Juhász and Horányi (1995), and Krivov *et al.* (1996a,b).

For Deimos ejecta, $W = 0.033$, $A = 0.0014$, $\tilde{L} = 0$, and

$$C = 7.684 \left(\frac{1\ \mu\text{m}}{r_{\rm g}} \right),$$

where we have assumed that $\rho_{\rm g} = 2.0$ g cm^{-3} and $Q_{\rm pr} = 1.0$. For grains smaller than about 100 μm, C is large and we can neglect A and W—at least for the evolution of e and $\phi_\odot$. The martian oblateness has a serious effect on the particle's inclination for particles of this size, though, as is seen in the above references. We are also restricted to grains larger than ≈ 1 μm, since electromagnetic forces from the solar wind strongly influence smaller grains. Deimos grains with $1\ \mu\text{m} \lesssim r_{\rm g} \lesssim 100\ \mu\text{m}$, however, are primarily perturbed by radiation pressure.

On the left-hand side of Fig. 3, we plot orbital eccentricity as a function of time for 80- and 20-μm dust particles launched from Deimos. On the right-hand side we show the corresponding phase portraits, curves of constant $\mathscr{K}$ plotted in polar coordinates (with $e \cos \phi_\odot$ along the x-axis and $e \sin \phi_\odot$ along the y-axis). In each phase portrait, the circle which passes through (0, 0) corresponds to the eccentricity trace which satisfies $e = 0$ at $t = 0$, and other curves correspond to different initial conditions. The phase portraits allow us to see, at a glance, how all other initial conditions $(e, \phi_\odot)$ will evolve. For a given initial e and $\phi_\odot$, the orbit travels clockwise along a nearly circular path in $e \cos \phi_\odot$–$e \sin \phi_\odot$ space. For the RP problem, it can be shown that the time of circulation is nearly 1 planetary year when radiation pressure is weak. The period decreases for more highly perturbed orbits (Juhász and Horányi 1995, Krivov *et al.* 1996a,b, Richter and Keller 1995).

Depending on the initial conditions, the solar angle may either rotate ($\mathscr{K}(e, \phi_\odot) < 1$) or librate ($\mathscr{K}(e, \phi_\odot) > 1$). Grains initially on nearly circular orbits are close to the boundary between these two types of motion; if the initial condition lies to the right of the origin in Figs. 3c and 3d, then the solar angle librates through a limited range of values; otherwise it rotates through a full 360°.

From the structure of Eq. (10), we can show that curves of constant $\mathscr{K}$ are, in general, nested ellipses with their long axes oriented parallel to the $e \sin \phi_\odot$ axis (Fig. 3d). For weak radiation pressure ($C \ll 1$), the curves are nearly circles (Fig. 3b). In the general case, all curves enclose the fixed point $(e_{\rm RP}, 0)$, have ellipticities which depend only on the value of C, and are centered on points dependent on both C and $\mathscr{K}$. In Fig. 3, the invariance of the curves to reflection through the x-axis is a general property of the full Hamiltonian (Eq. (9)).

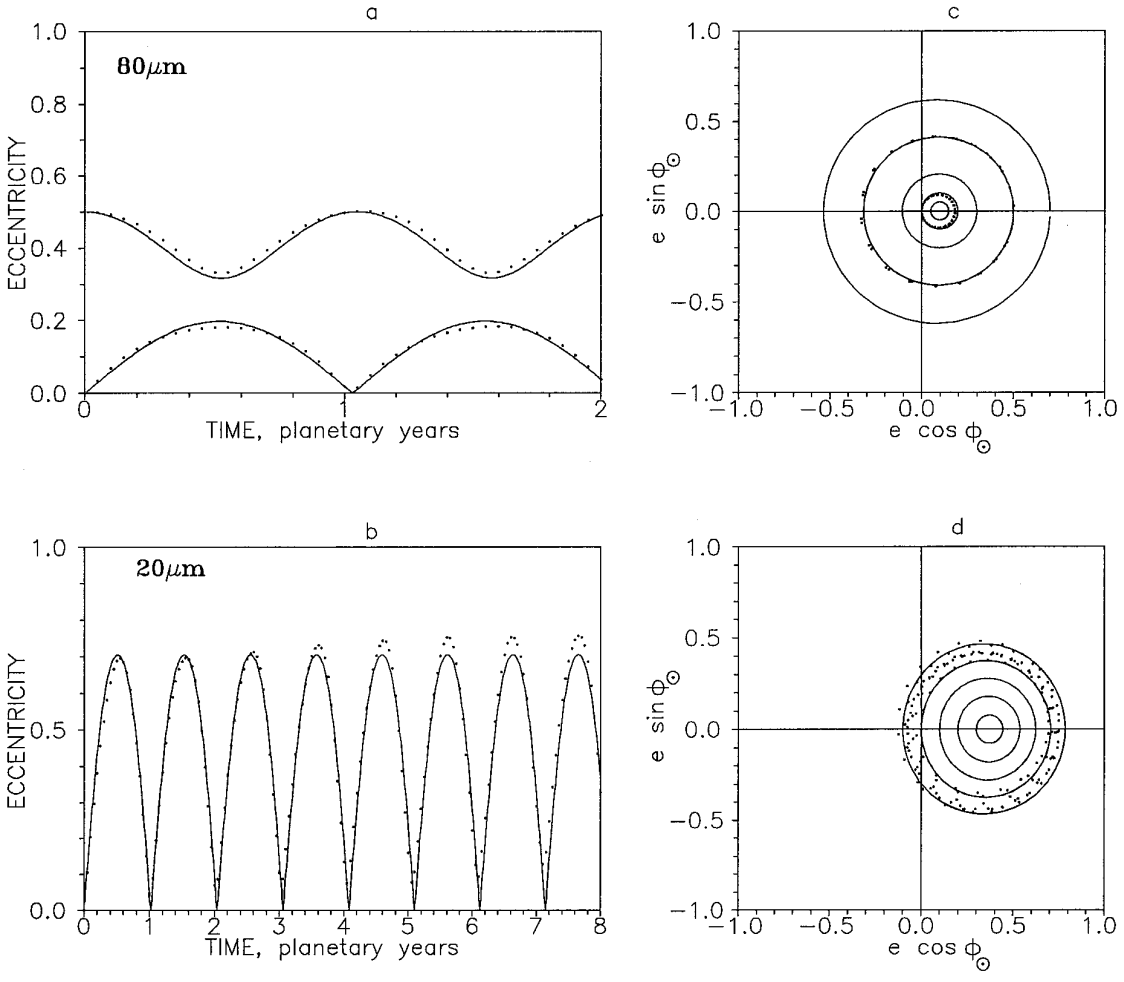

FIG. 3. Dynamical evolution of 80- and 20-μm Deimos ejecta under radiation pressure alone. (a) and (b) compare integrations of the simplified 2D system (7) (solid lines) to full 3D integrations of $\mathbf{F} = m\mathbf{a}$ (dotted lines). (c) and (d) are phase portraits determined from level curves of the Hamiltonian (solid lines) with 3D numerical integrations superimposed (points). The phase portraits are simple polar plots of eccentricity versus the solar angle. The single local maximum of $\mathscr{H}$, P_{RP}, is clear in both phase portraits. The position of P_{RP} depends on particle size, but the topology of the phase space does not. Despite the significant martian obliquity ($\sim$25°) and the large inclinations developed by Deimos' ejecta (from $\sim$6° for $r_g = 80$ μm to $\sim$30° for $r_g = 20$ μm), the phase topology and main dynamical features are still evident in the 3D simulations. The appreciable scatter of points in (d) is due primarily to the unmodeled effects of large inclinations.

We can also evaluate the maximum eccentricity for an initially circular orbit using the integral (10). Inserting (9) into the equation $\mathscr{H}(0, 0) = \mathscr{H}(e_{\max}, 0)$ results in

$$e_{\max} = \frac{2C}{1 + C^2}, \quad C < 1. \tag{17}$$

Equation (17) is our analytical result for the shape of Fig. 2a; since C is proportional to the inverse of the grain size (Eqs. (2) and (3)) then, for small C, $e_{\max}$ is also inversely proportional to the grain size. The eccentricity varies between zero and $e_{\max} \approx 2e_{\mathrm{RP}}$ for weak radiation pressure ($C \ll 1$). In this limit, e_{RP} is equivalent to the parameter e_{forced} discussed by Hamilton (1996).

When radiation pressure is strong, Eq. (17) implies that $e_{\max}$ can be large enough that dust particles strike the central body. For distant orbits, however, the orbit-averaged approximation begins to break down, and changes to e within a single orbit often allow dust particles to avoid immediate collisions. In such cases, prograde-to-retrograde transitions can occur, with particles periodically altering the sense of their revolutions about the central body (see, e.g., Figs. 10 and 11 from Hamilton and Burns (1992)). Nevertheless, particles on such orbits usually collide with the central planet after only a short amount of time.

3.2. Solar Tides Only (*ST*)

When grains are large and far from the planet, the solar tidal force is the dominant perturbation and we can take $C = W = \tilde{L} = 0$. In this case, the Hamiltonian for the solar tidal term is a function of only e and $\cos(2\phi_\odot)$, and hence the solution curves are symmetric about both the $e \cos \phi_\odot$ and $e \sin \phi_\odot$ axes. Examination of Eq. (9) shows that the level curves are broadest along the $e \cos \phi_\odot$ axis, which indicates that distant orbits will attain maximum eccentricities when their pericenters or apocenters are aligned with the Sun. The point (0, 0) is a fixed point, and the second of Eqs. (7) shows that all additional fixed points come in pairs and must lie along the $e \cos \phi_\odot$ axis. Indeed, with $C = W = \tilde{L} = 0$, there are either zero or two additional stationary points for Eqs. (11)-(13) over the physical range $0 < e < 1$. These are given by $P_{ST1} = (e_{ST}, 0)$ and $P_{ST2} = (e_{ST}, \pi)$ with e_{ST} obtained from $\mathscr{H}_0(e) = -6Ae$. We find that

$$e_{ST} = \left(1 - \frac{1}{36A^2}\right)^{1/2}, \quad A > \frac{1}{6}. \tag{18}$$

For values of A less than 1/6, the tidal perturbations to $\phi_\odot$ in Eqs. (7) cannot compete with the -1 from solar motion, and hence no equilibria are possible. In this case, the fixed point at (0, 0) is a maximum, and the solar angle regresses through a full 360°. As A is increased above 1/6, two new extrema P_{ST1} and P_{ST2} split from the origin $e = 0$ and move outward along the $e \cos \phi_\odot$ axis. The corresponding equilibrium orbits maintain constant eccentricities and keep their pericenters pointed either toward or away from the Sun. Consideration of the second derivatives of $\mathscr{H}$ shows that, when they do exist, P_{ST1} and P_{ST2} are local maxima and (0, 0) is a saddle. In this case, librating solar angles can occur for certain initial conditions.

We choose Elara at $164R_J$, the outermost of Jupiter's prograde satellites, to illustrate typical dynamics when the solar tidal force is the dominant perturbation. This is a good approximation for millimeter and larger grains ejected from Elara's surface and for Elara itself. We have $C = W = \tilde{L} = 0$ and $A = 0.045$; since $A < 1/6$, there are no fixed points with $e \neq 0$. Figure 4c shows that level curves of the Hamiltonian are ovals centered on (0, 0). The fact that the solar angle regresses means that motion along the level curves proceeds in the clockwise direction.

In Figure 4a, we compare integrations of the simplified 2D system (7) (solid lines) to full 3D integrations of $\mathbf{F} = m\mathbf{a}$ (dotted lines). The short-period oscillations visible in the $\mathbf{F} = m\mathbf{a}$ integrations occur at Elara's orbital period; these oscillations do not show up in our 2D integrations since the latter depend on orbit-averaged equations (Eqs. (7)). Orbit-averaging becomes a less accurate approximation as perturbing forces become larger—in this case at greater distances from the planet.

No stable satellite in the solar system satisfies $A > 1/6$, the restriction for the phase topology with three fixed points. Elara has the largest A among the prograde satellites, and Jupiter's Sinope, with $A = 0.129$, is the champion of the retrograde satellites. Numerical simulations show that initially circular prograde orbits are stable out to about half of the Hill radius (Hamilton and Burns 1991), which implies that $A = 0.15$. This is interestingly close to the change in the phase topology at $A \approx 0.167$.

3.3. Radiation Pressure and the Solar Tidal Force (*RP + ST*)

Both radiation pressure and solar gravity are strong perturbation forces on distant material tens to hundreds of micrometers in size around planets, or millimeters to centimeters around asteroids (Hamilton and Burns 1992). When both forces are important, the perturbation equations (7) are more complicated. Setting $\partial\mathscr{H}/\partial\phi_\odot = 0$ first (Eq. (13)), we see that three types of equilibrium points are possible: $\phi_\odot = 0$, $\phi_\odot = \pi$, or $e \cos \phi_\odot = -C/10A$. The third possibility, however, makes $\partial\mathscr{H}/\partial e < 0$ for all e, and therefore does not allow fixed points. Solutions in the first two cases are given by $\partial\mathscr{H}(e, \phi_\odot)/\partial e = 0$, which we rewrite as $F_\pm(e) = 0$, where

$$F_\pm(e) = \pm C \frac{\sqrt{1 - e^2}}{e} + 6A\sqrt{1 - e^2} - 1, \tag{19}$$

the plus sign indicates $\phi_\odot = 0$, and the minus sign denotes $\phi_\odot = \pi$. The equation $F_\pm(e) = 0$ can be reduced to a quartic with a complicated closed-form solution, but instead we investigate the derivative of the right-hand side with respect to e. For $F_+(e)$, $dF_+(e)/de$ is a monotonically decreasing function of the eccentricity over the relevant range $0 < e < 1$. Since $F_+(0) \to \infty > 0$ and $F_+(1) = -1 < 0$, there is exactly one fixed point with $\phi_\odot = 0$ for all values of A and C: $P_3 = (e_3, 0)$. The second derivative test shows that P_3 is always a local maximum and inspection of $F_+(e)$ indicates that the eccentricity e_3 is larger than both e_{RP} and e_{ST}.

The derivative of $F_-(e)$ changes sign once, indicating a single maximum at $e = e' = (C/6A)^{1/3}$; since $F_-(0) \to -\infty$ and $F_-(1) = -1$ are both negative, there are at most two fixed points when $\phi_\odot = \pi$. The number of fixed points is determined by the value of $F_-(e)$ at its maximum (i.e., $F_-(e')$); setting this to zero yields $6A = (1 + C^{2/3})^{3/2}$. If this equality is satisfied there is a single fixed point, for smaller A no fixed points exist, and for larger A there are two fixed points. The condition for the existence of fixed points is more stringent here than when the solar tidal force acts alone; it reduces to the previously derived $A >$

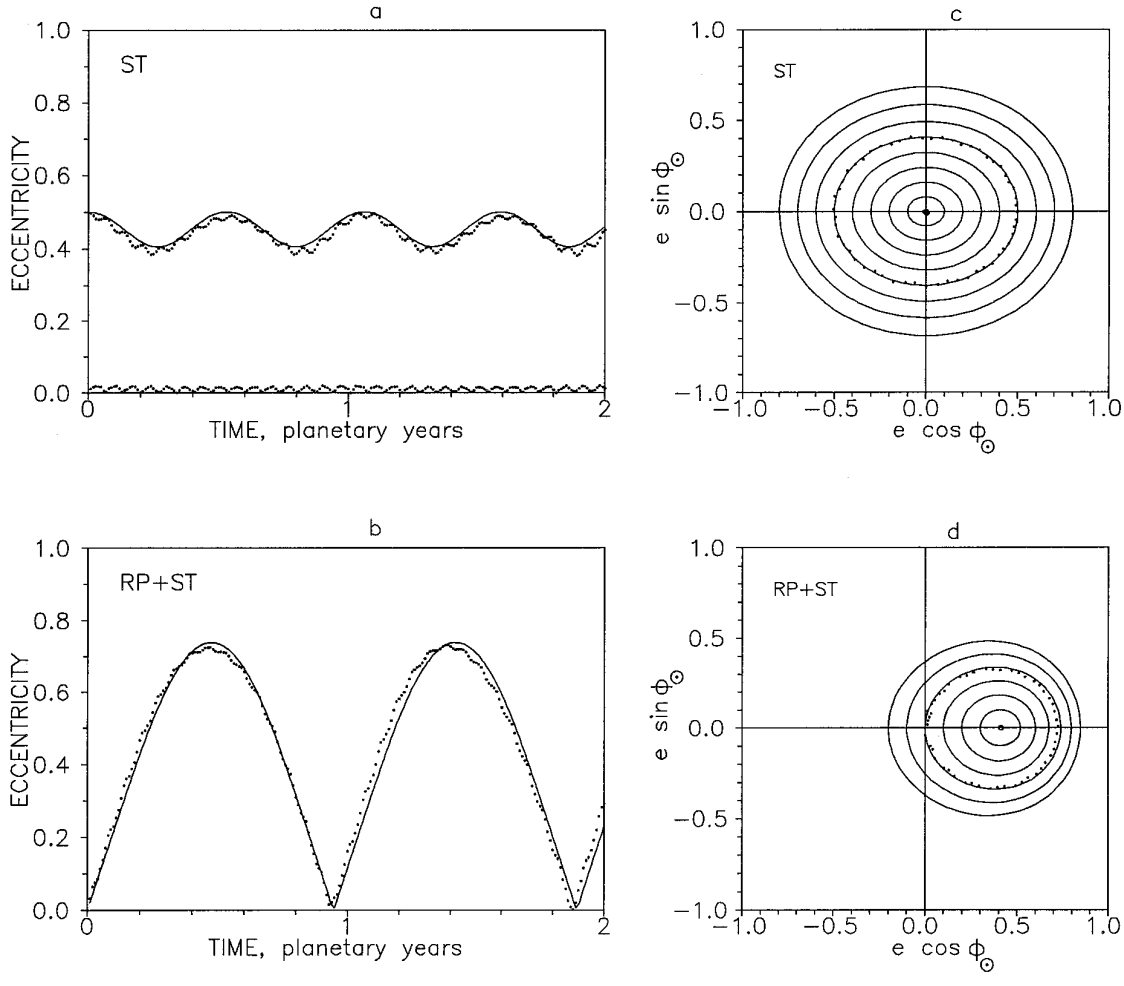

FIG. 4. Dynamical evolution of material from the outer prograde jovian moon Elara. The moon's 28° orbital inclination has been artificially set to zero, and solid and dotted curves are as detailed in the legend to Fig. 3. In (a) and (c), only the solar tidal force acts (ST problem), while (b) and (d) are appropriate for a 10-μm grain for which radiation pressure is also important (RP + ST problem). The left graphs give the eccentricity as a function of time, and the right ones depict phase portraits. The stationary point seen in (d) is the local maximum P_3; it moves toward the origin (0, 0) as radiation pressure weakens (c).

1/6 in the weak radiation pressure limit. When the two fixed points P_4 and P_5 exist, the eccentricities satisfy $e_4 < e' < e_5$ and it can be shown that P_4 is always a saddle point while P_5 is always a local maximum. The properties of these stationary points are summarized in Table I.

TABLE I
Fixed Points in the RP + ST Problem

Stationary point	Eccentricity restriction	Existence	Type
$P_3 = (e_3, 0)$	$e_3 > e_{RP}, e_3 > e_{ST}$	Always	Maximum
$P_4 = (e_4, \pi)$	$e_4 \leq (C/6A)^{1/3}$	$6A \geq (1 + C^{2/3})^{3/2}$	Saddle
$P_5 = (e_5, \pi)$	$e_5 \geq (C/6A)^{1/3}$	$6A \geq (1 + C^{2/3})^{3/2}$	Maximum

Dust from Elara is well approximated by the RP + ST problem; we have $W = \tilde{L} = 0$, $A = 0.045$, and

$$C = 3.420 \left(\frac{1\ \mu\text{m}}{r_g} \right),$$

assuming that $Q_{pr} = 1.0$ and $\rho_g = 1.0$ g cm^{-3}.

We consider 10-μm grains: since $6A < (1 + C^{2/3})^{3/2}$, there is only a single equilibrium point $P_3 = (e_3, 0)$, as follows from Table I. Figure 4b indicates that the 2D equations for 10-μm grains (solid line) give a good approximation of the actual motion of Elara dust grains (dotted line). The phase trajectories obtained from the Hamiltonian equations for these particles are shown in Fig. 4d. Figure 4d is similar to Fig. 3d because C is much larger than A.

Nevertheless, the curves in Fig. 4d are noticeably more elongated in the x direction than those in Fig. 3d due to the presence of solar tides. The solar angle may either rotate through a full 360° or librate through a limited range of angles depending on the initial e and $\phi_\odot$. Grains with very low initial eccentricities are near the boundary between these two types of motion as in the case when radiation acts alone (Section 3.1 and Fig. 3d).

4. THE NEAR ZONE

The opposite limiting case of the full set of equations is achieved when particle orbits lie within several planetary radii of the central object. In this zone, the solar tidal force is negligible, so we set $A = 0$. But planetary oblateness perturbations and, for small grains, electromagnetic and radiation pressure forces can all influence a particle's motion. We have in general, therefore, the RP + J2 + EM problem, which we consider in much the same way as in the previous section. We start with the simplest subcases when the three forces (RP, J2, and EM) act alone. The first of these, RP alone, has already been examined in Section 3.1, so we proceed to the other two cases. Note, however, that the oblateness and electromagnetic forces originate from the planet and have nothing to do with the Sun. It is, therefore, a bit unusual to study these forces in a frame rotating with the solar motion, and we do so only for logical completeness.

4.1. *Oblateness Only* (*J2*), *Electromagnetism Only* (*EM*), *and Both Forces Together* (*J2 + EM*)

The analytic solution to the orbit-averaged J2 problem shows that elliptical orbits keep their size and shape as they slowly rotate at a constant rate in space (Danby 1988). With our formalism, we take $A = C = \tilde{L} = 0$ and $W \neq 0$, and find that the Hamiltonian (9) is independent of $\phi_\odot$. From the last fact, it immediately follows that all trajectories in the $e\cos\phi_\odot$–$e\sin\phi_\odot$ space are origin-centered circles $e = \text{Const}$. If $W \geq 1$, then fixed points are absent and the solar angles of all orbits precess (rotate counterclockwise in the phase portraits). If $0 < W < 1$, then singular points (Eq. (11)) form all along the circle

$$e = e_{J2} = \sqrt{1 - W^{1/2}} = \text{Const.} \tag{20}$$

Physically, this means that for $e = e_{J2}$ the precession rate of the pericenter forced by planetary oblateness exactly matches the Sun's mean motion. Thus an orbit with $e = e_{J2}$ maintains a constant angle to the Sun–planet line. For $e > e_{J2}$, the apses line rotates counterclockwise with respect to the solar direction ($\phi_\odot$ precesses), while for $e < e_{J2}$, motion is clockwise (the solar angle regresses). The existence of a circle of equilibrium points is a degenerate situation arising from the fact that the oblateness term is independent of $\phi_\odot$. The addition of even weak radiation pressure or solar tides breaks this degeneracy.

The EM problem ($A = C = W = 0$, $\tilde{L} \neq 0$) is nearly identical to the J2 one. Again, the Hamiltonian is a function of only the eccentricity, so all level curves are circles centered on the origin. The equilibrium points exist only if $0 < \tilde{L} < 1$, and the equilibrium condition (Eq. (11)) yields circles of radius

$$e = e_{EM} = \sqrt{1 - \tilde{L}^{2/3}} = \text{Const.} \tag{21}$$

The sense of rotation in the phase space is counterclockwise (the solar angle precesses) for $e > e_{EM}$ and clockwise ($\phi_\odot$ regresses) for $e < e_{EM}$. Precession also occurs for all $\tilde{L} > 1$ and regression for all negative $\tilde{L}$.

When oblateness and Lorentz forces are both important, the problem is mathematically more complex, although no fundamentally new features arise. Here $A = C = 0$, $W \neq 0$, and $\tilde{L} \neq 0$. Examination analogous to that used in the two previous cases results in the following: If $W + \tilde{L} < 1$, there exists a family of stationary points along the circumference of a circle with radius

$$e = e_{J2EM} = \sqrt{1 - \varepsilon^2} = \text{Const,} \tag{22}$$

where ε is the solution of the equation

$$\varepsilon^4 - \tilde{L}\varepsilon - W = 0. \tag{23}$$

Consideration of this function and its derivative shows that there is only a single root satisfying $0 < e < 1$. Thus for a given W and $\tilde{L}$, there is at most one eccentricity at which the precession rates exactly balance the motion of the Sun. If $W + \tilde{L} \geq 1$, then no stationary points exist in the relevant range $0 < e < 1$.

4.2. *Radiation Pressure and Oblateness* (*RP + J2*)

Now we turn to the case when radiation pressure and oblateness act simultaneously (this case was first explored by Krivov *et al.* (1996b)). We take $A = \tilde{L} = 0$ and, since the two degenerate cases of no oblateness and no radiation pressure have already been considered in Section 3, we also require that $C > 0$ and $W > 0$.

As follows from Eqs. (11)–(13), all stationary points within $0 < e < 1$ have the form

$$(e_*, 0), \quad (e_{**}, \pi), \tag{24}$$

where e_* and e_{**} are, respectively, the roots of the equations

$$\mathscr{H}_0(e) = -C, \quad \mathscr{H}_0(e) = C. \tag{25}$$

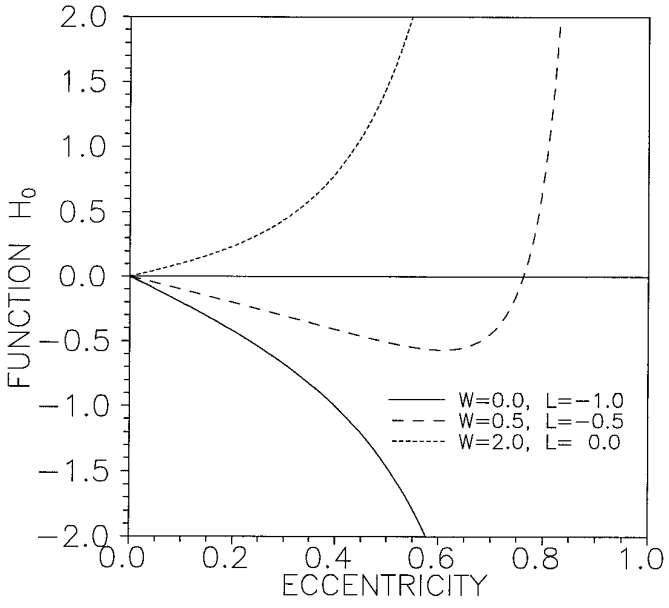

FIG. 5. The function $\mathcal{H}_0(e)$ (see Eq. (12)) for various $\tilde{L}$ and W. The intersections of a curve $\mathcal{H}_0(e)$ with straight lines $\mathcal{H}_0(e) = \pm C$ determine stationary points of the Hamiltonian $\mathcal{H}(e, \phi_\odot)$.

Before discussing the roots of these two equations, we first summarize the properties of the function $\mathcal{H}_0(e)$, which is given by Eq. (12) with $\tilde{L} = 0$. The function has the limits

$$\mathcal{H}_0(0) = 0, \quad \lim_{e\to 1} \mathcal{H}_0(e) = +\infty,$$

and there is a single root $\mathcal{H}_0(e_{J2}) = 0$ in the range $0 < e_{J2} < 1$, with e_{J2} given by Eq. (20). This root exists only if $0 < W < 1$—there are no roots when $W \geq 1$. Does $\mathcal{H}_0(e)$ have an extremum? Setting $d\mathcal{H}_0(e)/de = 0$ yields a single minimum at

$$e_- = \sqrt{1 + 2W - (4W^2 + 5W)^{1/2}} \tag{26}$$

which exists only if $0 < W < 1$. No extrema exist when $W \geq 1$. So for $W > 1$, $\mathcal{H}_0(e)$ has no roots and no extrema; hence it increases monotonically like the dotted curve in Fig. 5. For the case when $0 < W < 1$, $\mathcal{H}_0(e)$ has one root and one minimum like the dashed curve in Fig. 5. These properties of $\mathcal{H}_0$ allow us to determine the number of roots of Eqs. (25) although we are unable to solve for them analytically. It follows that the first of Eqs. (25) has two roots, e_3 and e_4, with the associated equilibrium points

$$P_3 = (e_3, 0), \quad P_4 = (e_4, 0) \tag{27}$$

if $\mathcal{H}_0(e_-) < -C$; one root $e_3 = e_4$ if $\mathcal{H}_0(e_-) = -C$; and no roots if $\mathcal{H}_0(e_-) > -C$ (imagine the intersection of lines of constant $\mathcal{H}_0(e)$ with the dashed curve in Fig. 5). The existence of two roots requires that radiation pressure be relatively weak. The second of Eqs. (25) always has one root e_5, with the associated stationary point

$$P_5 = (e_5, \pi). \tag{28}$$

The properties of the three stationary points P_3, P_4, and P_5 are summarized in Table II.

Dust grains launched from the martian moon Phobos provide a typical example of dynamics governed by the two parameters C and W. We consider the motions of Phobos ejecta in the micrometer to millimeter size range, assume that $\tilde{L} = 0$, and neglect $A = 0.00035$ in comparison to W. The relevant parameters are

$$W = 0.8290, \quad C = 4.858 \left(\frac{1\,\mu\text{m}}{r_g}\right),$$

with $\rho_g = 2.0$ g cm^{-3} and $Q_{pr} = 1$. Figure 6 shows the numerically determined eccentricity histories for grains of different sizes launched on initially circular orbits. The 2D integrations presented here agree well with 3D $\mathbf{F} = m\mathbf{a}$ simulations done elsewhere (Hamilton 1996, Ishimoto 1996, Krivov *et al.* 1996a,b). Note the pronounced differences in the shapes and periods of the curves, especially the marked change between 331-μm grains and 335-μm grains. This difference is responsible for the sharp drop in eccentricity with increasing particle size seen in Fig. 2's middle panel. This effect was recently found by several authors (Hamilton 1996, Ishimoto 1996, Krivov *et al.* 1996a,b) and shown to be quite stable by means of numerical integrations of more realistic 3D equations of motion.

Figure 7 shows the set of phase portraits determined from Eq. (9); the curve passing through the origin of each phase portrait has a corresponding eccentricity curve in Fig. 6. These phase plots have one of three different topological types which are distinguished by the number of stationary points: three (Figs. 7a–7d), two (Fig. 7e), or one (Fig. 7f). In the case where three fixed points exist (Figs. 7a–7d), the two trajectories that pass through the saddle P_4 have infinite periods and together are called the separatrix. Figure 8 shows the eccentricities of the equilibrium points as a function of particle size; these curves were obtained

TABLE II
Fixed Points in the RP + J2 Problem

Stationary point	Eccentricity restriction	Existence	Type
$P_3 = (e_3, 0)$	$e_3 \leq e_-$	$C \leq -\mathcal{H}_0(e_-)$	Maximum
$P_4 = (e_4, 0)$	$e_- \leq e_4 < e_{J2}$	$C \leq -\mathcal{H}_0(e_-)$	Saddle
$P_5 = (e_5, \pi)$	$e_5 > e_{J2}$	Always	Minimum

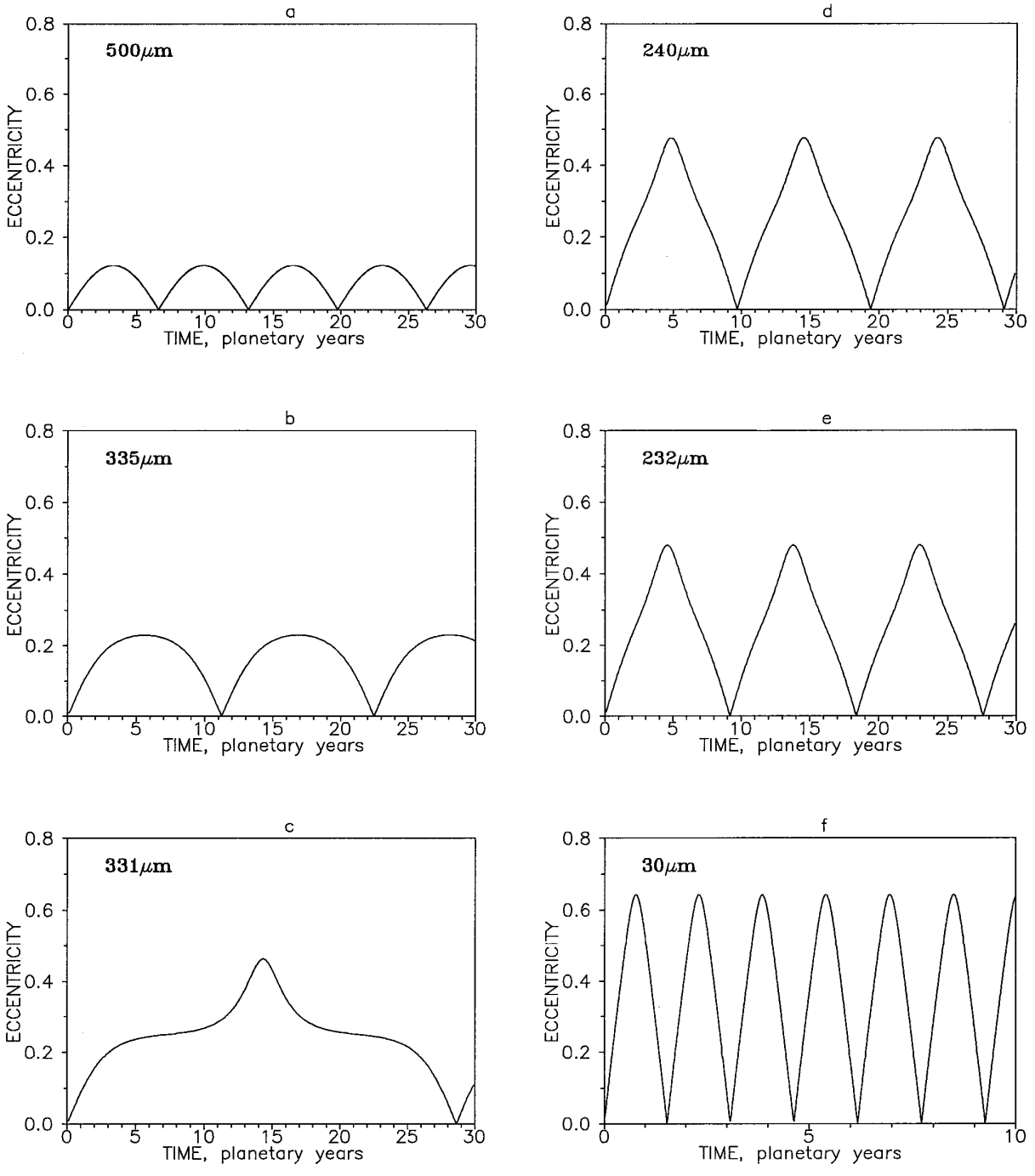

FIG. 6. Dynamical evolution of Phobos ejecta, as an illustration of the RP + J2 problem. Depicted is the evolution of eccentricity for initially circular orbits of different-sized grains. These plots were calculated from the 2D model.

by solving Eqs. (25) numerically for various values of C. The plot clearly shows the transition from a single equilibrium point, through the degenerate case of two points, to three equilibrium points.

Since satellites are the sources for orbital debris and most satellites in the Solar System orbit along nearly circular paths, we pay particular attention to the trajectory that passes through the origin of the phase plots—the $e = 0$ trajectory. Changes in the behavior of this trajectory, rather than changes in the number of fixed points, account for the large differences among Fig. 6's eccentricity histories. Numerical simulations and Eqs. (7) show that radiation

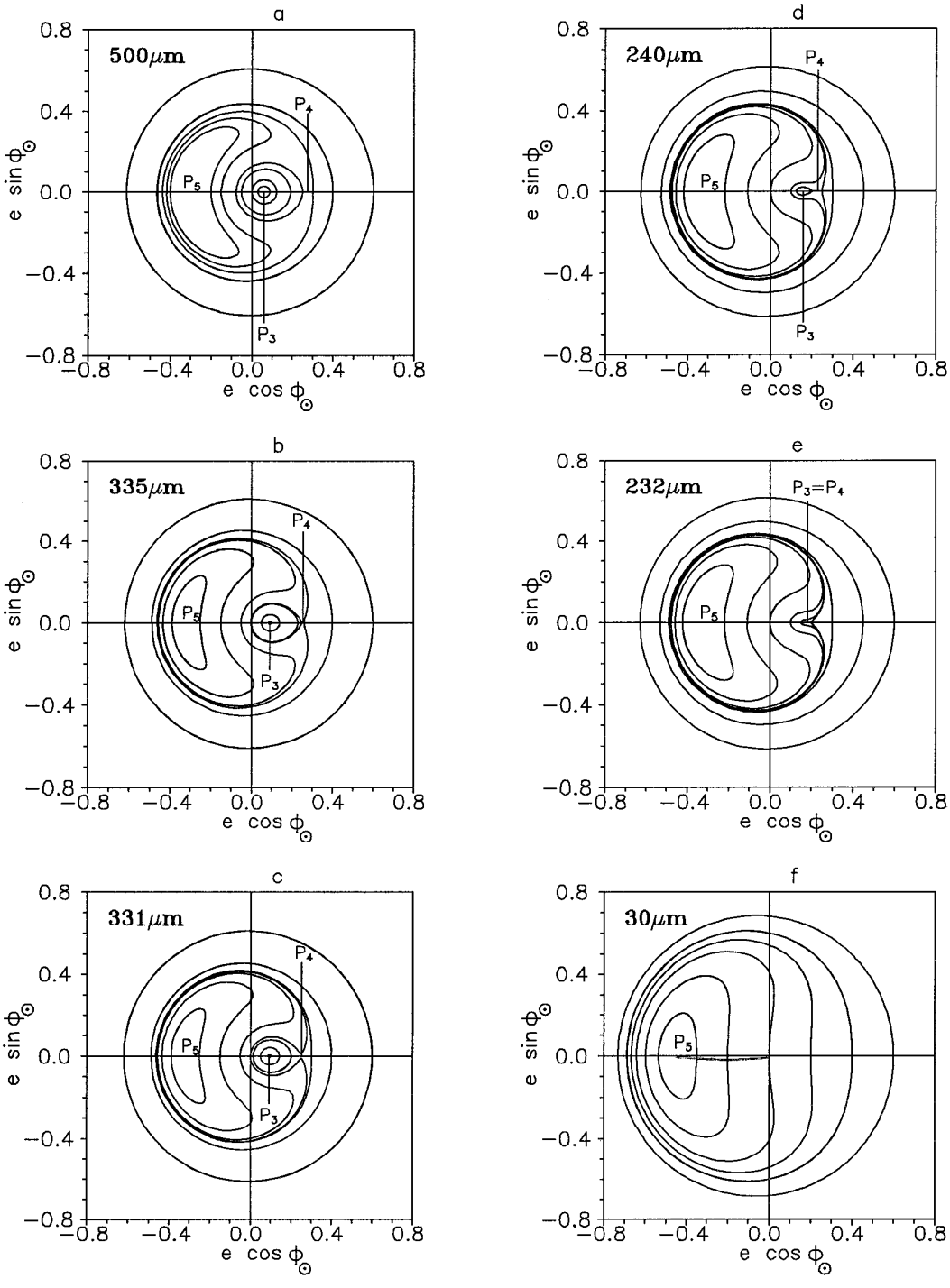

FIG. 7. Dynamical evolution of Phobos ejecta: phase portraits (eccentricity versus solar angle) in polar coordinates. The grain sizes are the same as those in Fig. 6 and the sequence of phase portraits presents examples of the different types from Table III.

pressure causes the solar angle of an initially circular orbit to spin rapidly to $P_1 = (0, \pi/2)$; thus all trajectories leaving the origin must travel initially upward in $e \cos \phi_\odot$–$e \sin \phi_\odot$ space. They return to the origin from below, i.e., through $P_2 = (0, 3\pi/2)$. For some phase portraits, the $e = 0$ trajectory reaches its maximum eccentricity when $\phi_\odot = 0$, while for others it occurs when $\phi_\odot = \pi$. In the former case, the $e = 0$ trajectory encloses the fixed point P_3 and the solar angle librates around $\phi_\odot = 0$ (Figs. 7a and 7b), while in the latter it encloses P_5 and the solar angle librates about

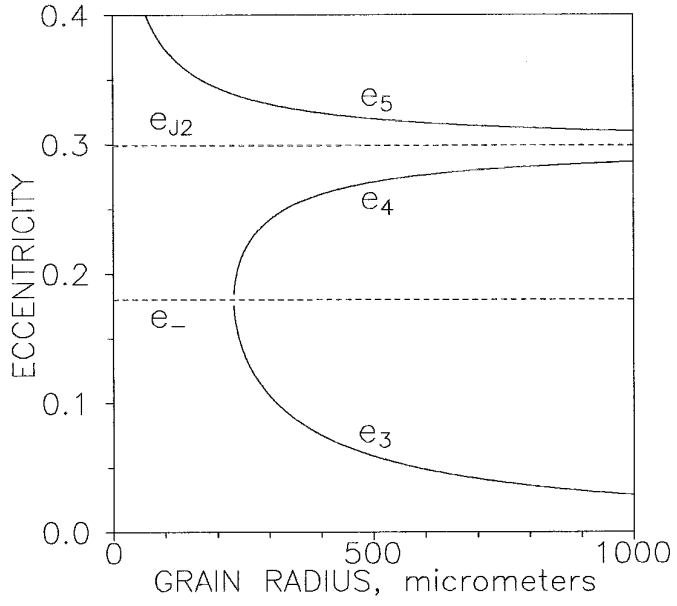

FIG. 8. Positions of the equilibrium points for Phobos ejecta as a function of particle size. For large sizes, radiation pressure is weak and the equilibrium points e_4 and e_5 are close to e_{J2} (Eq. (20)). At a grain size of 232 μm, the equilibrium points e_3 and e_4 merge at e_- (Eq. (26)), and for smaller grains only the fixed point e_5 remains.

$\phi_\odot = \pi$ (Figs. 7c and 7d). Accordingly, we split the case with three fixed points into three subcases depending on whether the $e = 0$ trajectory encloses P_3, P_5, or both fixed points.

The five different types of phase portraits, two of which are degenerate, are given in Table III. For types I, II, and III, the Hamiltonian has three stationary points: a saddle (P_4) and two centers (P_3 and P_5). For type I portraits, the $e = 0$ trajectory surrounds the center P_3 and the solar angle librates about $\phi_\odot = 0$ (Figs. 7a and 7b). In contrast, for type III portraits the $e = 0$ trajectory surrounds the center P_5 and the solar angle librates about $\phi_\odot = \pi$ (Figs. 7c and 7d). The transition between types I and III occurs at the degenerate type II portrait. At this point, the $e = 0$ trajectory is identical to the separatrix which passes through the saddle P_4 (between Figs. 7b and 7c). The transition is not associated with changes in the number of stationary points and cannot be derived from a local analysis of the phase space. Type V portraits have a single center P_5 (Fig. 7f), and type IV is the degenerate transition between types III and V. The type IV portrait represents a *bifurcation of stationary points*, i.e., the emergence of the two stationary points P_3 and P_4 (Fig. 7e).

These five types of phase portraits bear an uncanny resemblance to the phase space topologies near first-order mean-motion resonances (see Borderies and Goldreich 1984, Malhotra 1992, Rasio *et al.* 1993), with the solar angle playing the role of the resonant angle. The resemblance comes from similarities between the equations governing each system. The major difference, however, is that mean-motion resonances strongly affect an orbit's semimajor axis, while the secular forces studied here do not.

It is not difficult to calculate parameter values at which the two degenerate portraits occur. The $e = 0$ trajectory corresponds to the separatrix when the fixed point $P_4(e_4, 0)$ and the origin $P_1(0, \pi/2)$ lie along the same integral curve; hence

$$\mathcal{H}(e_4, 0) = \mathcal{H}(0, \pi/2). \tag{29}$$

In addition, from the definition of P_4 we have

$$\mathcal{H}_0(e_4) = -C. \tag{30}$$

Using Eq. (12), Eqs. (29)–(30) may be rewritten explicitly:

$$\begin{aligned} \sqrt{1 - e_4^2} + Ce_4 + \frac{W}{3(1 - e_4^2)^{3/2}} &= 1 + \frac{W}{3}, \\ \frac{e_4}{\sqrt{1 - e_4^2}}\left[\frac{W}{(1 - e_4^2)^2} - 1\right] &= -C. \end{aligned} \tag{31}$$

These two equations can be solved numerically for the two unknowns C and e_4. Using values for Phobos, and taking $C > 0$ to avoid the trivial solution $e_4 = C = 0$, we find $C = 0.01466$ and $e_4 = 0.25$. The value of C implies that $r_g \approx 331.5$ μm and e_4 is the value of the eccentricity at the

TABLE III
Classification of Phase Portraits in the RP + J2 Problem

Portrait type	Stationary points	$e = 0$ trajectory	Figures
I	P_3, P_4, P_5	Surrounds P_3	7a and 7b
II	P_3, P_4, P_5	Surrounds P_3 and P_5	Between 7b and 7c
III	P_3, P_4, P_5	Surrounds P_5	7c and 7d
IV	$P_3 = P_4, P_5$	Surrounds P_5	7e
V	P_5	Surrounds P_5	7f

bottom of the jump in Fig. 2. This definition of e_4 is similar to, but more precise than, the definition of $e_{\rm crit}$ by Hamilton (1996). The critical grain size agrees with that found by Krivov *et al.* (1996a,b) and also with Hamilton's (1996) $s_{\rm crit}$ when the differences in assumed grain density are folded in.

The parameter values at the bifurcation of stationary points can be found analytically. The bifurcation takes place when $\mathscr{H}_0(e)$ reaches its minimum (see the dashed curve in Fig. 5) so that

$$\left.\frac{d\mathscr{H}_0(e)}{de}\right|_{e_-} = 0. \tag{32}$$

Equation (32) reduces to a quadratic equation with the relevant root given by Eq. (26). For Phobos, $W = 0.829$, so $e_- = 0.180$. Using $e_- = e_3$ (see Fig. 8) and the definition of P_3, we find $C = -\mathscr{H}_0(e_-) = 0.0210$ and $r_{\rm g} \approx 232\ \mu$m.

4.3. Radiation Pressure and Electromagnetism (*RP + EM*)

The RP + EM problem ($A = W = 0$, $C \neq 0$, $\tilde{L} \neq 0$) is nearly identical to the RP + J2 case. As above, the stationary points of the Hamiltonian are given by Eqs. (24) and (25), but here the function $\mathscr{H}_0(e)$ satisfies

$$\mathscr{H}_0(0) = 0, \quad \lim_{e\to 1} \mathscr{H}_0(e) = \begin{cases} -\infty & \text{if } \tilde{L} < 0 \\ +\infty & \text{if } \tilde{L} > 0. \end{cases}$$

The only root of $\mathscr{H}_0(e_{\rm EM})$ in $0 < e_{\rm EM} < 1$ is given by Eq. (21) and exists only if $0 < \tilde{L} < 1$; otherwise there are no roots. The function $\mathscr{H}_0(e)$ has a single extremum (a minimum e_-). The position of the minimum is obtained by setting $d\mathscr{H}_0(e)/de = 0$, which can be rewritten as a cubic equation in e^2:

$$(1 - e^2)^{3/2} - \tilde{L}(1 + 3e^2) = 0. \tag{33}$$

As in the J2 case, this equation has only one solution in the range $0 < e < 1$ if $0 < \tilde{L} < 1$, and has no solutions otherwise. When $0 < \tilde{L} < 1$, there are three equilibrium points P_3, P_4, and P_5 whose properties are analogous to those in the RP + J2 problem. For $\tilde{L}$ outside this range, only a single root is present, as can be seen graphically from the dotted and solid curves of Fig. 5.

4.4. Radiation Pressure, Oblateness, and Electromagnetism (*RP + J2 + EM*)

We have now arrived at the most general case for motion of dust grains near planets. The inclusion of all three forces considered separately above greatly complicates the mathematics, but does not alter the general appearance of the phase portraits discussed in the previous two sections. In the analysis that follows, we assume $A = 0$ and the strict inequality $W > 0$. As in the RP + J2 problem, the stationary points of the Hamiltonian are given by Eqs. (24) and (25). The function $\mathscr{H}_0(e)$ satisfies

$$\mathscr{H}_0(0) = 0, \quad \lim_{e\to 1} \mathscr{H}_0(e) = +\infty.$$

We now look at the derivative $d\mathscr{H}_0(e)/de$ in $0 < e < 1$ to determine how many extrema the function $\mathscr{H}_0(e)$ may have. The equation $d\mathscr{H}_0(e)/de = 0$ can be rewritten in the form

$$f_1(e^2) = f_2(e^2), \tag{34}$$

with

$$\begin{aligned} f_1(e^2) &\equiv (1 - e^2)^2 - W(1 + 4e^2), \\ f_2(e^2) &\equiv \tilde{L}(1 + 3e^2)\sqrt{1 - e^2}. \end{aligned} \tag{35}$$

The function $f_1(e^2)$ is monotonically decreasing from $f_1(0) = 1 - W$ to $f_1(1) = -5W$. The properties of $f_2(e^2)$ depend on the sign of $\tilde{L}$. If $\tilde{L} > 0$ ($\tilde{L} < 0$), $f_2(e^2)$ monotonically increases (decreases) from $f_2(0) = \tilde{L}$ to the maximum (minimum) $f_2(5/9) = 16/9\,\tilde{L}$ and then decreases (increases) to $f_2(1) = 0$.

There are four special cases to consider. First, for positive $\tilde{L}$, there is a single solution to Eq. (34) when $W + \tilde{L} < 1$ and no solution when $W + \tilde{L} > 1$. This is suggested from the values of $f_1(e^2)$ and $f_2(e^2)$ and their derivatives at the endpoints of the eccentricity range, but can be proven by also considering the curvatures (given by the second derivatives). Thus when $\tilde{L} > 0$, the function $\mathscr{H}_0(e)$ has at most one extrema. For negative $\tilde{L}$, we find the same behavior: one solution to Eq. (34) when $W + \tilde{L} < 1$ (Fig. 5's dashed curve) and no solution when $W + \tilde{L} > 1$ (Fig. 5's dotted curve). So the function $\mathscr{H}_0(e)$ is either monotonic or has a single extrema as plotted for several examples in Fig. 5. As with the RP + J2 and RP + EM cases considered above, when $\mathscr{H}_0(e)$ is monotonic there is a single solution to Eq. (25), and when the function has one extremum there can be one, two, or three fixed points.

So we find that the properties of the fixed points P_3, P_4, and P_5 in the RP + J2 + EM problem are quite similar to those in the simpler RP + J2 and RP + EM problems outlined in the previous subsections. In particular, no new types of phase portraits are introduced by the inclusion of all forces and Table III is still valid in this more general case.

An ideal example where radiation pressure, oblateness, and electromagnetism are simultaneously important is Saturn's E ring, a tenuous dusty sheet formed by particles launched from Enceladus. Substituting numerical values relevant for dust from Enceladus into Eqs. (2)–(4) we find

TABLE IV
Critical Values of (r_g, Φ_g) for Particles Released from Enceladus

Transition of $e = 0$ trajectory (type II)		Bifurcation of fixed points (type IV)	
r_g	Φ_g	r_g	Φ_g
0.70	−2.75	0.70	−2.60
0.80	−3.53	0.80	−3.35
0.90	−4.40	0.90	−4.18
1.00	−5.36	1.00	−5.11
1.10	−6.40	1.10	−6.12
1.20	−7.55	1.20	−7.22
1.30	−8.75	1.30	−8.41

$$W = 12.61,$$
$$C = 0.6575\left(\frac{1\ \mu\text{m}}{r_g}\right), \tag{36}$$
$$\tilde{L} = 13.78\left(\frac{\Phi_g}{5\ \text{V}}\right)\left(\frac{1\ \mu\text{m}}{r_g}\right)^2,$$

where we have taken $\rho_g = 1.0$ g cm^{-3} and $Q_{pr} = 1.0$. Paralleling the derivations of Section 4.2, we generalize the equations which determine when the $e = 0$ trajectory corresponds to the separatrix (Eq. (31)) to

$$\sqrt{1-e_4^2} + Ce_4 + \frac{W}{3(1-e_4^2)^{3/2}} + \frac{\tilde{L}}{2(1-e_4^2)} = 1 + \frac{W}{3} + \frac{\tilde{L}}{2},$$
$$\frac{e_4}{\sqrt{1-e_4^2}}\left[\frac{W}{(1-e_4^2)^2} + \frac{\tilde{L}}{(1-e_4^2)^{3/2}} - 1\right] = -C. \tag{37}$$

The general equations for the bifurcation of stationary points (Eq. (32)) are

$$W(1+4e_3^2) - (1-e_3^2)^2 = -\tilde{L}(1+3e_3^2)\sqrt{1-e_3^2},$$
$$C = -\mathscr{H}_0(e_3). \tag{38}$$

After substitution of (36) into (37), the latter system will contain three unknown parameters: r_g, Φ_g, and e_4. Since there are two equations in (37), there exists a one-parametric family of solutions. The same is true for the system in (38). Table IV contains the critical values of (r_g, Φ_g) calculated numerically from (36)–(38).

We see that, with a negative potential of several volts (typical for E ring grains), both critical values occur near $r_g \sim 1\ \mu$m. Since we expect behavior similar to that shown in Figs. 6 and 7, we perform full integrations of $\mathbf{F} = m\mathbf{a}$ for grains with near-critical values. In Fig. 9, we show the variations of eccentricity with time for grains of radius 2.0, 1.0, and 0.5 μm for two plausible voltages (−5.6 and −5.2 V). The evolution of the solar angle for the same sizes and potentials is shown in Fig. 10, and the phase portraits in the $e\cos\phi_\odot$–$e\sin\phi_\odot$ plane are given in Fig. 11.

By showing integrations of the full equations of motion, we stress again that adding moderate inclinations and refraining from using an orbit-averaged approximation leads only to slight scattering of phase curves, but is unable to destroy the basic topology. Figures 11a and 11d show type V portraits (Table III, Fig. 7f). Oblateness dominates electromagnetism, the function $\mathscr{H}_0(e)$ looks like the dotted curve in Fig. 5 (since $W + \tilde{L} > 1$), and there is a single fixed point P_5. The solar angle precesses (Figs. 10a and 10d), so motion is counterclockwise along the level curves of Figs. 11a and 11d.

The $e = 0$ trajectories in (b) and (e) of Figs. 9–11 are close to—and on opposite sides of—the separatrix (Table IV). Figure 11b's phase portrait is of type I (*cf.* Fig. 7a) and Fig. 11e's is of type III (*cf.* Fig. 7d). Note that some orbits in Figs. 11b and 11e do not close, indicating the effects of non-zero inclinations in some cases and insufficient integration times in others. The $e = 0$ trajectory can cross the separatrix as a result of slight changes in Φ_g (*cf.* Figs. 11b and 11e), in r_g (*cf.* Figs. 2c and 11d–11f), or even in the orbital semimajor axis a. This phenomenon was first reported by Hamilton (1993).

Figures 11c and 11f are of Type I. Here, electromagnetism dominates oblateness, the function $\mathscr{H}_0(e)$ looks qualitatively like the dashed curve in Fig. 5 (since $W + \tilde{L} < 0$), and there are three fixed points. The stationary points P_4 and P_5 occur very close to $e = 1$, so they are not apparent in these phase plots. The solar angle regresses (Figs. 10c and 10f), so motion is clockwise along the level curves of Figs. 11c and 11f. There is more scatter in these panels because the electromagnetic force is a strong perturbation and the orbit-averaged approximation is rather poor. Furthermore, the dust grain in Fig. 11c is very close to a 16:3 resonances between the grain's orbital period and the eccentricity oscillations, which accounts for Fig. 11c's odd appearance.

Interestingly, observations of the E ring's color show that it is composed of a monosize distribution of particles dominated by $r_g = 1.0 \pm 0.3\ \mu$m (Showalter *et al.* 1991), a finding that has been recently reconfirmed during the 1995 ring plane crossing observations. These grains have parameters near the critical values (Table IV), and hence attain very high eccentricities (*cf.* Fig. 9e), as was first pointed out by Horányi *et al.* (1992). Particles with high orbital eccentricities create a broad ring, in agreement with observations, and collide with Enceladus at high velocities in 20–100 years. Hamilton and Burns (1994) argue that

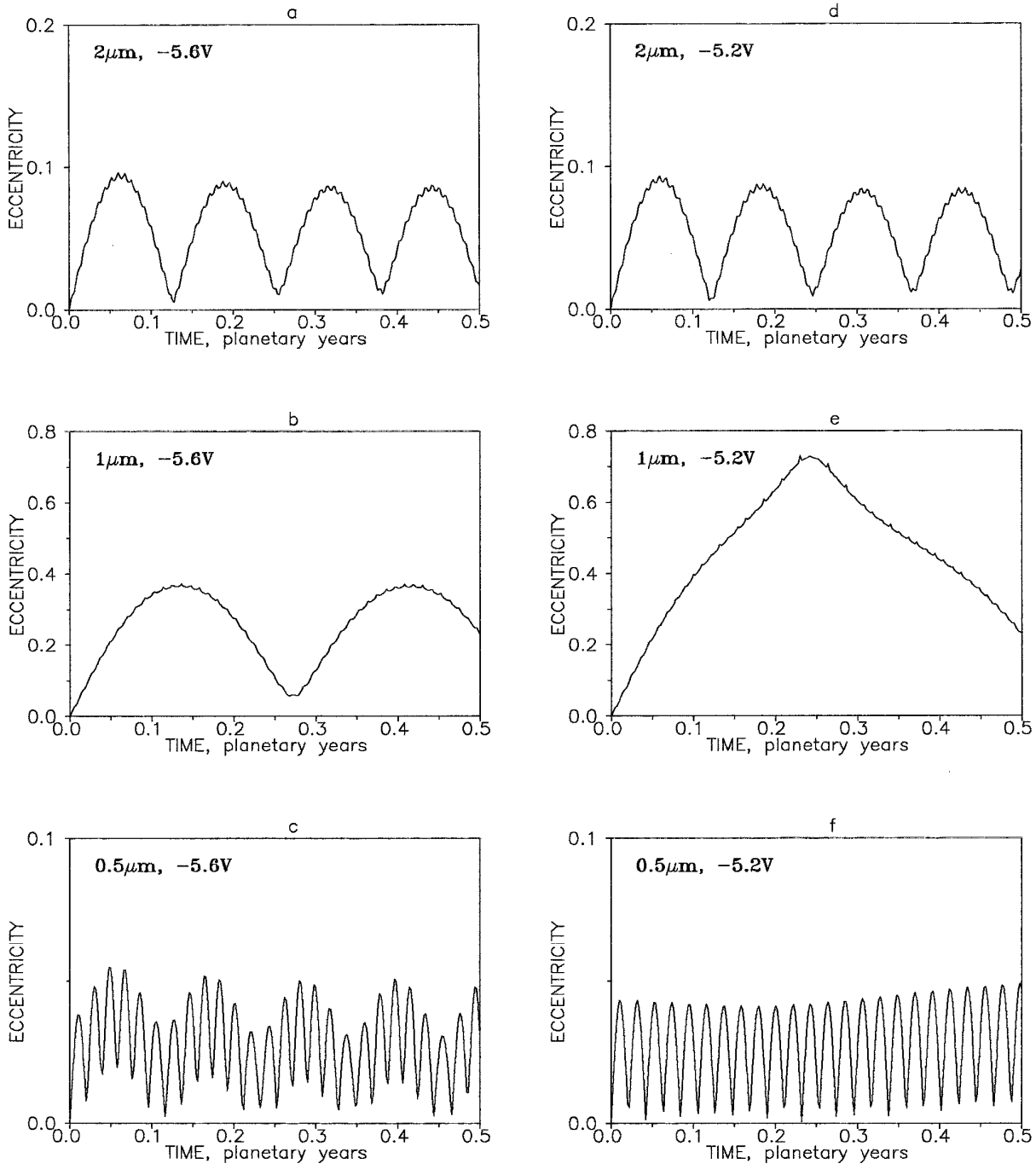

FIG. 9. Dynamical evolution of Enceladus' ejecta, as an illustration of the RP + J2 + EM problem. Evolution of eccentricity for initially circular orbits. Three typical sizes (2.0, 1.0, and 0.5 μm) and two typical voltages (−5.6 and −5.2 V) were chosen. The data were obtained from numerical integration of full 3D equations of motion.

these energetic collisions eject material off Enceladus and sustain the E ring at its observed optical depth.

5. THE INTERMEDIATE ZONE

As in the previous sections, we first consider a special case before attempting the full system. The most important subcase applies to large objects at all distances from planets for which only gravitational forces are important.

5.1. Oblateness and Solar Tides (J2 + ST)

For millimeter and larger objects, we set $C = \tilde{L} = 0$ and look for roots of Eqs. (11)–(13). Since the Hamiltonian is

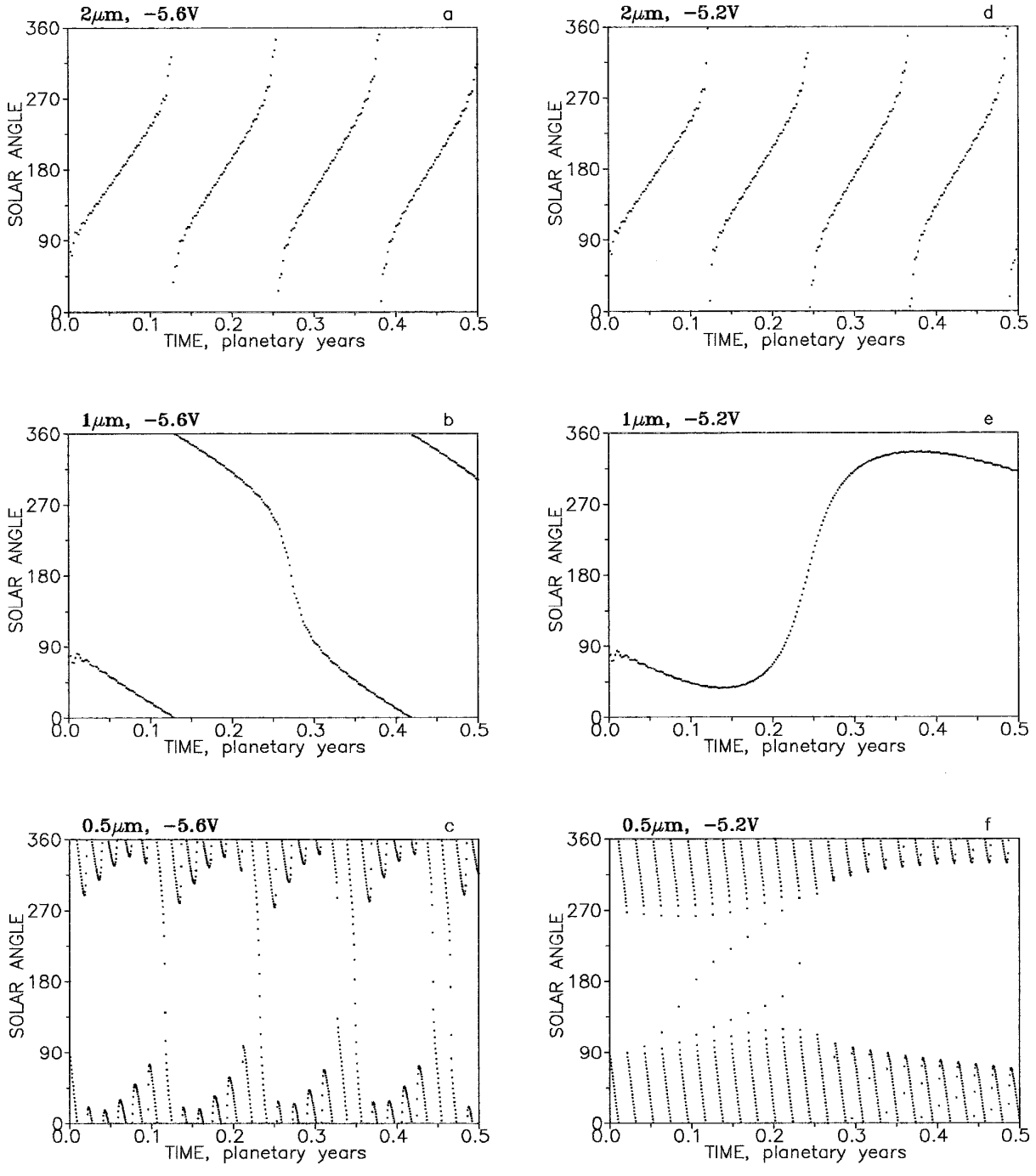

FIG. 10. Dynamical evolution of Enceladus' ejecta: solar angle as function of time. The sizes and voltages are the same as those in Fig. 9.

a function of e and $\cos(2\phi_\odot)$ only, as in Section 3.2, level curves will be mirror symmetric about both the $e\cos\phi_\odot$ and the $e\sin\phi_\odot$ axes. Setting $\partial\mathcal{H}/\partial\phi_\odot = 0$ first (Eq. (13)), we find that equilibrium points with $\phi_\odot = 0$, $\pi/2$, π, and $3\pi/2$ are all possible. Defining $\varepsilon = (1 - e^2)^{1/2}$, $\partial\mathcal{H}/\partial e = 0$ (Eq. (13)) can be rewritten

$$F_-(\varepsilon) = W - \varepsilon^4 - 4A\varepsilon^5 = 0; \quad \phi_\odot = \pi/2, 3\pi/2 \qquad (39)$$

$$F_+(\varepsilon) = W - \varepsilon^4 + 6A\varepsilon^5 = 0; \quad \phi_\odot = 0, \pi. \qquad (40)$$

These are fifth-order polynomials for which there is no general solution. Inspection of $F_-(0) = W$, $F_-(1) = W - 1 - 4A$, and $\partial F_-(\varepsilon)/\partial\varepsilon$, however, allows us to conclude that Eq. (39) has no solution over the interval $0 < \varepsilon < 1$ when $W - 1 - 4A \geq 0$ and a single solution (two fixed points) when $W - 1 - 4A < 0$.

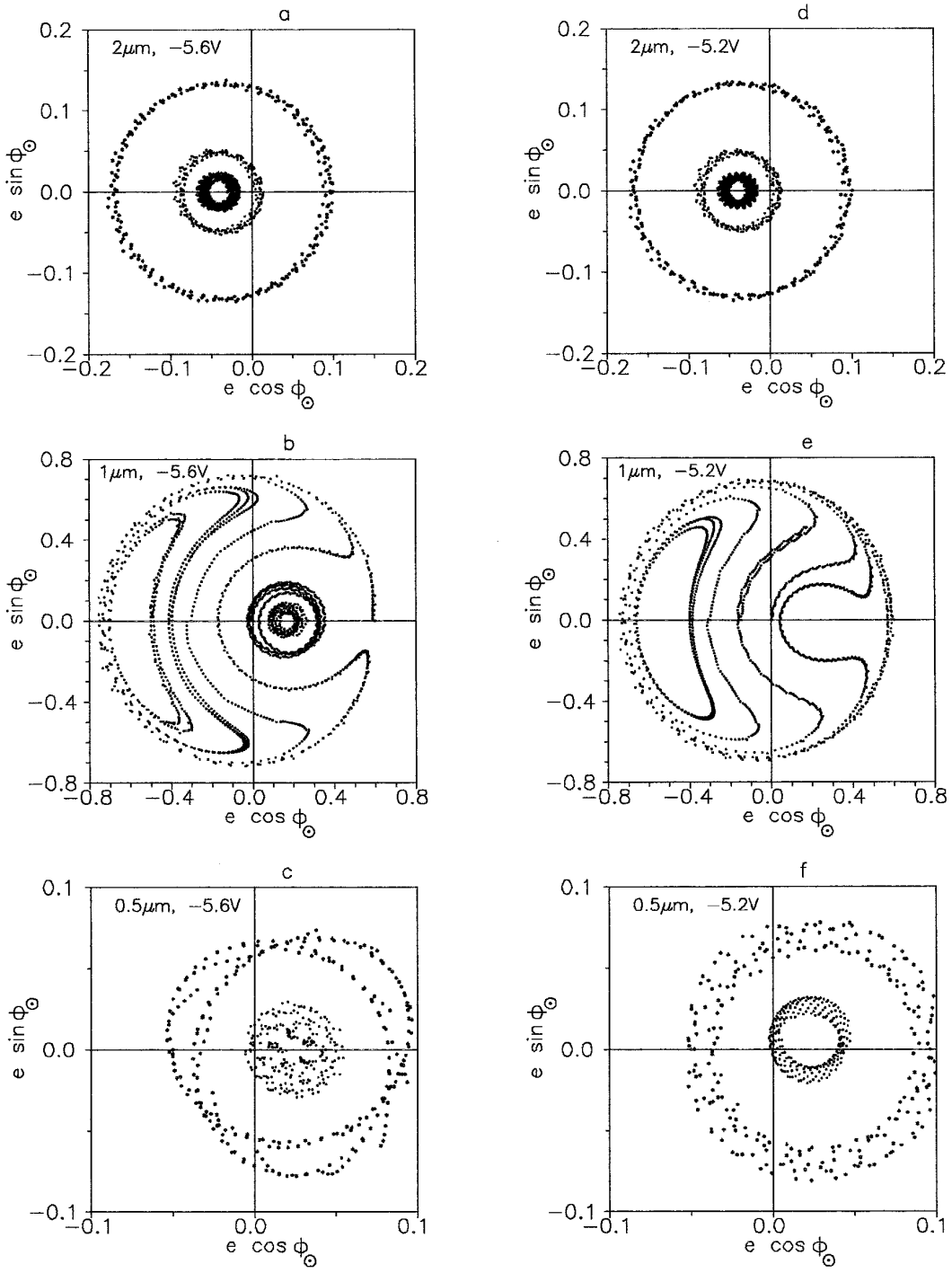

FIG. 11. Dynamical evolution of Enceladus' ejecta: phase portraits. The sizes and voltages are the same as those in Figs. 9 and 10. This sequence demonstrates the different nondegenerate portrait types from Table III: Type I (b, c, f), Type III (e), and Type V (a, d).

Equation (40) is a bit more complicated. Elementary analysis tells us that, if $A < 2/15$, the function $F_+(\varepsilon)$ is monotonically decreasing from $F_+(0) = W$ to $F_+(1) = W - 1 + 6A$. Consequently, if $A < 2/15$, then Eq. (40) has no solution when $W - 1 + 6A \geq 0$ and one solution when $W - 1 + 6A < 0$. If $A \geq 2/15$, the function first decreases from $F_+(0) = W$ to a minimum at $F_+(2/15A) = W - (2/15A)^4/5$ and then increases to $F_+(1) = W - 1 + 6A$. If $W - 1 + 6A < 0$, then there is always a single solution. For $W - 1 + 6A > 0$, Eq. (40) has no solution if

$W > (2/15A)^4/5$, one solution if $W = (2/15A)^4/5$ (degenerate case), and two solutions if $W < (2/15A)^4/5$. From this follows that a necessary, but not sufficient, rule for the existence of two solutions to Eq. (40) is $A > 2/15$ and $W < 1/5$. These inequalities are satisfied only for objects very far from the central planet.

These observations allow us to conclude that, besides the fixed point at (0, 0), phase portraits in the J2 + ST problem can have either (i) no fixed points, (ii) two fixed points (with $\phi_\odot = \pi/2, 3\pi/2$), (iii) four fixed points (with $\phi_\odot = 0, \pi/2, \pi, 3\pi/2$—this case can be degenerate), or (iv) six fixed points (two with $\phi_\odot = \pi/2, 3\pi/2$ and four with $\phi_\odot = 0, \pi$).

There are a number of cases in the solar system for which both oblateness and solar tides are important. A classic example is Saturn's satellite Iapetus with $A = 0.0055$ and $W = 0.001$. In fact, the effective W is actually higher due to perturbations from the massive interior satellite Titan. The phase portrait in this case is of type iii with four fixed points, but these are all very near $e = 1$. Since $e_{\text{Iapetus}} = 0.03$, the fixed points have no influence on the orbit of Iapetus.

A highly elliptical orbit like that of Shoemaker–Levy 9 (SL 9) (with $A \sim 0.13$, $W \sim 1 \times 10^{-6}$, $e \sim 0.99$) provides another example. Near the pericenter, SL9 was strongly affected by oblateness, while near the apocenter solar tides dominated the perturbations. Orbits similar to SL9's may have phase portraits with type ii, iii, or iv topologies; in addition, the large orbital eccentricity is comparable to the eccentricities of the fixed points, which makes the dynamics interesting. A caveat is that large and highly eccentric orbits push the limits of our orbit-averaged approximation.

5.2. *All Forces (ST + RP + J2 + EM)*

When all four forces are important, the perturbation equations (7) are very complicated. Setting $\partial \mathscr{H}/\partial \phi_\odot = 0$ first (Eq. (13)), we see that three types of equilibrium points are possible: $\phi_\odot = 0$, $\phi_\odot = \pi$, or $e \cos \phi_\odot = -C/10A$. Unlike the ST + RP case discussed in Section 3.3, there are cases when the off-axis equilibrium points do exist. An example, albeit an unphysical one, is given in Fig. 12. These off-axis points reduce to the $\phi_\odot = \pi/2$, $\phi_\odot = 3\pi/2$ equilibria discussed in Section 5.1 in the limit $C \to 0$.

In general, all of the topological types discussed in Sections 4.4 and 5.1 are possible, and there are almost certainly additional types. An exhaustive catalog of all possible topological types of this most general phase space is beyond the scope of this paper.

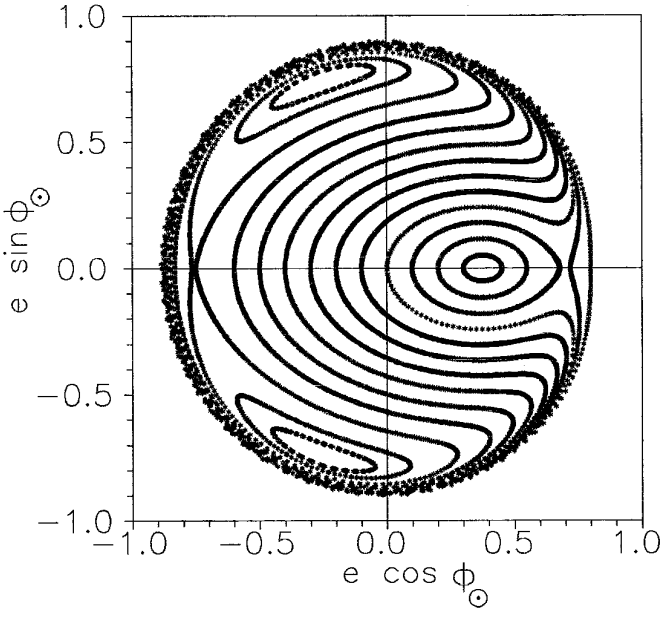

FIG. 12. A phase portrait with five nontrivial stationary points which provides an illustrative example of dynamical evolution when all four perturbation forces are important. The parameters are $C = 0.25$, $W = 0.8$, $A = 0.1$, and $\tilde{L} = -1.0$, and the five fixed points are given by $P_3 = (0.376, 0°)$, $P_4 = (0.697, 0°)$, $P_5 = (0.759, 180°)$, $P_6 = (0.786, 109°)$, and $P_7 = (0.786, 251°)$.

6. CONCLUSION

We have constructed a simple analytical model of a planetocentric motion of a dust grain influenced by four disturbing forces: solar gravity, solar radiation pressure, planetary oblateness, and electromagnetism. By exploiting a newly discovered integral of the motion we are able to reduce a system with two unknown functions of time to one with a single unknown function. Such a system can be easily characterized. Our approach is a reasonable approximation for many interesting problems in the Solar System. In addition to the applications discussed in this paper—Saturn's E ring, dust around Mars, and ejecta from the outer jovian and saturnian satellites—our method can also be applied to jovian ring particles, terrestrial space debris, lunar ejecta, artificial satellites with large area-to-mass ratios (Krivov and Getino 1995), and dust in the uranian and neptunian systems.

We have systematically explored the phase space in a number of special cases, analyzed its properties and structure, and used this information to approach a number of Solar System applications from a different angle. We find, from this exploratory work, that sharp changes in orbital eccentricity at a critical set of parameters occur quite commonly. These sharp changes, which we have seen for Phobos ejecta and for dust in Saturn's E ring, are very robust and are almost certainly important elsewhere in the Solar System.

ACKNOWLEDGMENTS

We are grateful to reviewers Matt Holman and Carl Murray for their critical readings of this manuscript.

REFERENCES

Borderies, N., and P. Goldreich 1984. A simple derivation of capture probabilities for the J + 1:J and J + 2:J orbit-orbit resonance problems. *Celest. Mech. Dynam. Astron.* **32,** 127–136.

Borderies, N., P. Goldreich, and S. Tremaine 1983. The variations in eccentricity and apse precession rate of a narrow ring perturbed by a close satellite. *Icarus* **53,** 84–89.

Burns, J. A., P. L. Lamy, and S. Soter 1979. Radiation forces on small particles in the solar system. *Icarus* **40,** 1–48.

Danby, J. M. A. 1988. *Fundamentals of Celestial Mechanics,* 2nd ed. Willmann-Bell, Richmond VA.

Duboshin, G. N. (Ed) 1976. *Reference Manual on Celestial Mechanics and Astrodynamics,* 2nd ed. Nauka, Moscow. [In Russian]

Hamilton, D. P. 1993. Motion of dust in a planetary magnetosphere: Orbit-averaged equations for oblateness, electromagnetic, and radiation forces with application to Saturn's E ring. *Icarus* **101,** 244–264; Erratum. *Icarus* **103,** 161.

Hamilton, D. P. 1994. A comparison of Lorentz, planetary gravitational, and satellite gravitational resonances. *Icarus* **109,** 221–240.

Hamilton, D. P. 1996. The asymmetric time-variable rings of Mars. *Icarus* **119,** 153–172.

Hamilton, D. P., and J. A. Burns 1991. Orbital stability zones about asteroids. *Icarus* **92,** 118–131.

Hamilton, D. P., and J. A. Burns 1992. Orbital stability zones about asteroids. II. The destabilizing effects of eccentric orbits and of solar radiation. *Icarus* **96,** 43–64.

Hamilton, D. P., and J. A. Burns 1994. Origin of Saturn's E ring: Self-sustained, naturally. *Science* **264,** 550–553.

Horányi, M., J. A. Burns, and D. P. Hamilton 1992. The dynamics of Saturn's E ring particles. *Icarus* **97,** 248–259.

Ishimoto, H. 1996. Formation of Phobos/Deimos dust rings. *Icarus* **122,** 153–165.

Juhász, A., and M. Horányi 1995. Dust torus around Mars. *J. Geophys. Res.* **100,** 3277–3284.

Krivov, A. V., and J. Getino 1995. Orbital evolution of high-altitude balloon satellites, *Astron. Astrophys.* in press.

Krivov, A. V., L. L. Sokolov, and V. V. Dikarev 1996a. Dynamics of Mars-orbiting dust. In *Proceedings of the IIIrd International Workshop on Positional Astronomy and Celestial Mechanics* (A. Lopez Garcia *et al.*, Eds.), Astronomical Observatory, University of Valencia, Spain, pp. 225–234.

Krivov, A. V., L. L. Sokolov, and V. V. Dikarev 1996b. Dynamics of Mars-orbiting dust: Effects of light pressure and planetary oblateness. *Celest. Mech. Dynam. Astron.*, in press.

Malhotra, R. 1992. Resonant orbital perturbations in the putative planetary system of PSR1257 + 12. *Nature* **356,** 583–585.

Mignard, F., and M. Hénon 1984. About an unsuspected integrable problem. *Celest. Mech. Dynam. Astron.* **33,** 239–250.

Peale, S. J. 1986. Orbital resonances, unusual configurations and exotic rotation states among planetary satellites. In *Satellites* (J. A. Burns and M. S. Matthews, Eds.), pp. 159–223. Univ. of Arizona Press, Tucson.

Rasio, F. A., P. D. Nicholson, S. L. Shapiro, and S. A. Teukolsky 1993. Orbital evolution of the PSR1257+12 planetary system. In *Planets around Pulsars* (J. A. Phillips, S. E. Thorsett, and S. R. Kulkarni, Eds.), *Astronomical Society of the Pacific Conference Series,* Vol. 36, pp. 107–119. Astronomical Society of the Pacific, San Francisco.

Richter, K., and H. U. Keller 1995. On the stability of dust particle orbits around cometary nuclei. *Icarus* **114,** 355–371.

Showalter, M. R., J. N. Cuzzi, and S. M. Larson 1991. Structure and particle properties of Saturn's E ring. *Icarus* **94,** 451–473.

Soter, S. 1971. The dust belts of Mars. Cornell Center for Radiophysics and Space Research Report 462.